Preprint submitted to the journal GEOPHYSICS.

An accurate analytical model for squirt flow in anisotropic porous rocks — Part 1: Classical geometry

Yury Alkhimenkov[123], **Beatriz Quintal**[12]

[1]*Institute of Earth Sciences, University of Lausanne, Lausanne, Switzerland*

[2]*Swiss Geocomputing Centre, University of Lausanne, Lausanne, Switzerland*

[3]*Faculty of Mechanics and Mathematics, Lomonosov Moscow State University, Moscow, 119899, Russia*

(December 3, 2021)

Running head: **An analytical model for squirt flow**

ABSTRACT

Seismic wave propagation in porous rocks that are saturated with a liquid exhibits significant dispersion and attenuation due to fluid flow at the pore scale, so-called squirt flow. This phenomenon takes place in compliant flat pores such as microcracks and grain contacts that are connected to stiffer isometric pores. Accurate quantitative description is crucial for inverting rock and fluid properties from seismic attributes such as attenuation. Up to now, many analytical models for squirt flow were proposed based on simplified geometries of the pore space. These models were either not compared with a numerical solution or showed poor accuracy. We present a new analytical model for squirt flow which is validated against a three-dimensional numerical solution for a simple pore geometry that has been classically used to explain squirt flow; that is why we refer to it as classical geometry. The pore space is represented by a flat cylindrical (penny-shaped) pore whose curved edge is fully connected to a toroidal (stiff) pore. Compared with correct numerical solutions, our analytical model provides very accurate predictions for the attenuation and dispersion across the whole frequency range. This includes correct low- and high-frequency limits of the stiffness modulus, the characteristic frequency, and the shape of the dispersion and attenuation curves. In a companion paper (Part 2), we extend our analytical model to more complex pore geometries. We provide as supplementary material Matlab and symbolic Maple routines to reproduce our main results.

INTRODUCTION

Wave propagation in fluid-saturated porous rocks exhibits energy loss, or attenuation, and velocity dispersion. Most of the attenuation and dispersion of seismic waves in such rocks are usually due to fluid flow taking place at various scales. At the pore scale, this energy loss is referred to as squirt flow (Mavko and Nur, 1975; Mavko and Jizba, 1991; Dvorkin et al., 1995; Pride et al., 2004; Gurevich et al., 2010; Müller et al., 2010; Pimienta et al., 2015a,b). Squirt flow occurs between interconnected pores due to different shapes or different orientations (Mavko et al., 2009; Müller et al., 2010). Many analytical models describing squirt flow have been suggested. These models explore squirt flow between interconnected compliant cracks (O'Connell and Budiansky, 1977; Palmer and Traviolia, 1980), between compliant cracks and stiff pores (Murphy et al., 1986; Mukerji and Mavko, 1994; Dvorkin et al., 1995; Pride et al., 2004; Gurevich et al., 2010; Collet and Gurevich, 2016) and between cracks and spheroidal pores (Xu, 1998; Chapman et al., 2002; Chapman, 2003; Jakobsen and Chapman, 2009). In real rocks, examples of compliant pores, which here are simply referred to as cracks, are microcracks and grain contacts. An overview of early theoretical studies on squirt flow is given by Jones (1986). Several experimental studies confirmed the importance of squirt flow at different frequency ranges, including sesimic frequencies (Mayr and Burkhardt, 2006; Adelinet et al., 2010; Mikhaltsevitch et al., 2015; Subramaniyan et al., 2015; Pimienta et al., 2015a,b; Chapman et al., 2019; Borgomano et al., 2019).

Numerically, squirt flow can be modeled by solving a set of equations describing coupled fluid-solid deformation (Zhang et al., 2010; Zhang and Toksöz, 2012; Quintal et al., 2016, 2019; Das et al., 2019; Alkhimenkov et al., 2020a,b; Lissa et al., 2020, 2021). Quintal et al. (2016, 2019) proposed a simplified numerical solution based on the linearized quasistatic Navier-Stokes equation. Alkhimenkov et al. (2020a) benchmarked this numerical solution using a published analytical model (Collet and Gurevich, 2016) under a specific scenario, while identifying and quantifying the causes of inaccuracies due to the assumptions used in the analytical model for scenarios corresponding to the described pore geometry. Guided by the numerical simulations presented in Alkhimenkov et al. (2020a), we develop an analytical model for squirt flow which allows us to accurately calculate the corresponding seismic dispersion and attenuation. This model does not have any fitting parameters and is in a very good agreement with three-dimensional numerical solutions across a wide frequency band. This article (Part 1) is focused on describing the analytical model for the classical geometry used in many previous studies: a penny shaped crack surrounded by a toroidal pore (Murphy et al., 1986; Gurevich et al., 2010; Collet and Gurevich, 2016). In a companion article (Part 2), we propose an analytical model for more complex geometries and investigate in further details the characteristic frequency of attenuation due to squirt flow. We provide Matlab and symbolic Maple routines to allow the reader to reproduce our main results and/or to obtain results for other material properties and pore sizes. The routines archive (v1.0) (Alkhimenkov and Quintal, 2021) is available from a permanent DOI repository (Zenodo) at `http://doi.org/10.5281/zenodo.5752570` (last access: 3 December 2021).

Importance of validating analytical models against numerical simulations

Rock physics relies on models that quantitatively describe certain physical concepts with predictive power. For squirt flow, all the models presented in the literature quantitatively describe the dispersion and attenuation based on many assumptions. Only recently, computational advances made it possible to directly compare analytical models against three-dimensional numerical solutions. As a result, it has been shown that certain analytical models are not accurate because some of their assumptions are not fulfilled even for idealized geometries (Alkhimenkov et al., 2020a).

We propose a simple and logical workflow which will make it possible to (i) benchmark published analytical models and (ii) ensure the quality of future models (Figure 1). There are five key steps. For a given physical concept, an analytical model for a simple geometry is considered (step 1). The solution can also be calculated numerically for the same simple geometry (step 2). The results predicted by the analytical model are benchmarked through the comparison with the numerical solution (step 3). If the analytical model can adequately describe the physics for a simple geometry, it then could be extrapolated for real rocks (step 4). This can be done by finding key parameters of the analytical models. If the analytical model for a simple geometry cannot describe the key features of the exact numerical solution for the same simple geometry, then this model shouldn't be applied to real rocks.

Up to now, "validation" of analytical models involved only steps 1 and 4. However, step 4 does not appropriately validate the analytical model because of obvious differences in corresponding geometries. Furthermore, other physical mechanisms, which were not accounted for in the analytical model, could have an important effect on the laboratory results. Indeed, "validation" against laboratory results usually require a number of fitting parameters. Therefore, validating analytical models against inherently accurate three-dimensional numerical simulations based on exact same model geometry and same physical mechanisms is of primary importance. Using a numerical solution helps to better understand the involved physical mechanism by evaluating the effect of key parameters as well as to improve the analytical model by testing assumptions.

Seismic attenuation and dispersion due to squirt flow

One measure of seismic P-wave attenuation is the so-called inverse quality factor $1/Q(\omega) = \mathrm{Im}\left(M(\omega)\right)/\mathrm{Re}\left(M(\omega)\right)$ (O'Connell and Budiansky, 1978), where $\omega = 2\pi f$ is the angular frequency (f is the frequency) and $M = K + 4/3G$ is the complex-valued P-wave modulus, K and G are the bulk and shear moduli, respectively. Throughout the article, by attenuation we imply the inverse quality factor.

We recall a brief overview of the physics based on previous analytical studies (Mavko and Jizba, 1991) with some additional information obtained from numerical simulations (Quintal et al., 2019; Alkhimenkov et al., 2020a,b; Lissa et al., 2020). In the physics of

squirt flow, the cause of energy dissipation is fluid pressure diffusion at the pore scale. An idealized rock model can be parameterized by three components: solid elastic matrix, isometric pores and thin compliant cracks (Figure 2). Pores and cracks are interconnected and saturated with a fluid. A passing seismic wave deforms the compliant cracks more than the stiff pores, which causes fluid pressure gradients in the cracks. This results in fluid pressure diffusion, sometimes referred to as local fluid flow or squirt flow, which strongly depends on the frequency of the propagating wave.

At low-frequencies, the fluid pressure becomes uniform throughout the pore space because there is enough time for it to equilibrate. This is called relaxed state. The effective elastic properties can be calculated by using Gassmann's equations (Gassmann, 1951) given that the elastic moduli of the dry frame are known. At low-frequencies, $1/Q$ is proportional to $\approx \omega^1$ according to numerical simulations for simple geometries (Alkhimenkov et al., 2020a). At intermediate frequencies, the fluid pressure gradients are at their maximum, which corresponds to the attenuation peak. The frequency at which the attenuation is at its maximum is called the characteristic frequency ω_c. At high frequencies, there is no time for fluid to flow or fluid pressure to diffuse between cracks and pores; cracks behave as hydraulically isolated from pores. This is called unrelaxed state. The slope of the high-frequency asymptote of the attenuation curve depends on the pore geometry (Alkhimenkov et al., 2020a,b). If the pore space is represented by a penny shaped crack connected to a toroidal pore, then $1/Q$ at high-frequencies is proportional to $\approx \omega^{-1/2}$. An evaluation of the high-frequency asymptote of $1/Q$ for more complex geometries is presented in the Part 2 of the present study.

THE ANALYTICAL MODEL

An analytical model for seismic attenuation and dispersion caused by squirt flow should, at least, accurately determine three key features: the low- and high-frequency limits for the elastic moduli and the characteristic frequency. To calculate the low-frequency limit, one needs the correct dry moduli of the rock and then use Gassmann's equations to obtain the moduli in the case of saturation with a fluid. To calculate the high-frequency limit, one needs the dry moduli of the rock where the crack normal compliance is zero and again use Gassmann's equations to obtain the moduli of the saturated rock. The characteristic frequency is directly related to the aspect ratio of compliant cracks and can be reasonably estimated. If these three parameters are determined, the dispersion and attenuation curves can be plotted using, for example, a standard linear solid (SLS) rheology. The disadvantage of the SLS model is that the resulting $1/Q$ is a symmetric curve if plotted in a bi-logarithmic scale, which is usually not the case for attenuation caused by squirt flow (Alkhimenkov et al., 2020a,b; Lissa et al., 2020).

The analytical model that we present here features the key components of previous analytical models for squirt flow (e.g., Dvorkin and Nur (1993); Mukerji and Mavko (1994);

Dvorkin et al. (1995); Gurevich et al. (2010); Glubokovskikh et al. (2016); Collet and Gurevich (2016)) but with several key modifications which make it accurate. The main building block of our analytical model is the so-called modified frame, which was originally introduced by Mavko and Jizba (1991). The modified frame represents a rock configuration where cracks are saturated with a fluid, whereas the isometric pores are dry. The development of our analytical model is shown in Figure 3. First, we calculate the moduli of the dry rock for two configurations: the dry rock containing the torus connected to the crack and the dry rock containing the torus connected to the crack with zero normal compliance (step 1, Figure 3). Then, we calculate the relaxation of the crack stiffness due to fluid pressure diffusion and obtain accurate values of the frequency-dependent moduli of the modified frame (step 2, Figure 3). Finally, we use Gassmann's equations to obtain the frequency-dependent moduli of the fully saturated medium (step 3, Figure 3).

General expressions

Let us consider the classical model for squirt flow presented in Figure 4, assuming a representative volume element (RVE) (for clarity, later in this article we will show slices of half of the models as in Figure 4b). The stiff isometric pore is represented by a torus and the penny-shaped crack is represented by a flat cylinder. The embedding medium consists of an elastic grain material described by a compliance tensor S^{g}_{ijkl}. The m-th inclusion (interconnected isometric pore and crack) is represented by a compliance contribution tensor $\mathbf{H}$ with components H^m_{ijkl}. The relation for the overall strain ϵ_{ij} can be written as

$$\epsilon_{ij} = S^{\mathrm{g}}_{ijkl}\sigma_{kl} + \Delta\epsilon_{ij} = S^{\mathrm{g}}_{ijkl}\sigma_{kl} + \sum_m H^m_{ijkl}\sigma_{kl}, \tag{1}$$

where σ_{kl} represents remotely applied stresses, $\Delta\epsilon_{ij}$ represents the extra strain due to the presence of the inclusion described by the $\mathbf{H}$-tensor. The components of the effective compliance tensor of a three-dimensional medium with inclusion(s) are

$$S^*_{ijkl} = S^{\mathrm{g}}_{ijkl} + \sum_m H^m_{ijkl}. \tag{2}$$

The expression 2 is exact and valid for a finite and infinitely extended RVE (Nemat-Nasser and Hori, 2013). The main assumption is that the grain material and inclusions are elastic and homogeneous. The compliance tensors can be complex functions of frequency (Hashin, 1970). In three-dimensions, the $\mathbf{H}$-tensors can be calculated exactly for ellipsoids by using the Eshelby result; in two-dimensions, exact results are known for several geometries (Kachanov and Sevostianov, 2018). In our particular case, in equations 1 and 2 $m = 1$ since we have only one inclusion. For our pore space geometry (Figure 4), no closed form expression of this $\mathbf{H}$-tensor exist, thus, we derive an approximation.

General expressions for our geometry

The key components of our model are illustrated in Figure 5. The effective compliance tensor with components S^*_{ijkl} for the dry model represented in Figure 5c can be written similarly to expression 2 (in Voigt notation),

$$[S^*_{mn}]_{\text{dry}} = S^{\text{g}}_{mn} + [H_{mn}]_{\text{dry}} \,. \tag{3}$$

The effective frequency-dependent compliance tensor with components $S^*_{ijkl}(\omega)$ for the fluid-saturated model is (Figure 5e)

$$[S^*_{mn}(\omega)]_{\text{sat}} = S^{\text{g}}_{mn} + [H_{mn}(\omega)]_{\text{sat}} \,. \tag{4}$$

The corresponding effective stiffness matrix for the saturated model is

$$[C^*_{mn}(\omega)]_{\text{sat}} = [S^*_{mn}(\omega)]^{-1}_{\text{sat}} \,. \tag{5}$$

The compliance matrix of an elastic grain material S^{g}_{mn} is frequency independent. We also introduce the compliance contribution matrix of the dry torus $\left[H^{\text{tp}}_{mn}\right]_{\text{dry}}$ and the compliance contribution matrix $[H_{mn}(\omega)]^{\text{MF}}$ of an inclusion represented by a dry torus connected to a crack saturated with a fluid (this compliance contribution can be used to obtain the moduli of the modified frame). By using expressions 3-5, several configurations of the model (illustrated in Figure 5) can be evaluated. For example, the effective compliance tensor for the dry model containing only the torus (Figure 5b) $[S^*_{mn}]^{\text{tp}}$ is

$$[S^*_{mn}]^{\text{tp}} = S^{\text{g}}_{mn} + \left[H^{\text{tp}}_{mn}\right]_{\text{dry}} \,. \tag{6}$$

The effective compliance matrix for the modified frame model (Figure 5d) is

$$[S^*_{mn}(\omega)]^{\text{MF}} = S^{\text{g}}_{mn} + [H_{mn}(\omega)]^{\text{MF}} \,. \tag{7}$$

Finally, the effective compliance matrix for the fluid-saturated model $[S^*_{mn}(\omega)]_{\text{sat}}$ can be calculated by applying anisotropic Gassmann's equations to expression 7 for each frequency. The result will be equivalent to that obtained via expression 4.

Some remarks

To calculate the resulting effective moduli, one needs to find the frequency-dependent compliance contribution matrix $[H_{mn}(\omega)]_{\text{sat}}$ of a saturated pore space represented by a torus connected to a flat cylinder (see expression 4). Equivalently, instead of finding $[H_{mn}(\omega)]_{\text{sat}}$ directly, we can find $[S^*_{mn}(\omega)]^{\text{MF}}$ and then obtain $[H_{mn}(\omega)]_{\text{sat}}$. Let's assume that a torus and a flat cylinder are disconnected and far from each other. We can represent the **H**-tensor in the form

$$[H_{mn}]_{\text{dry}} = \left[H^{\text{tp}}_{mn}\right]_{\text{dry}} + [H^{\text{cr}}_{mn}]_{\text{dry}} \,, \tag{8}$$

where $\left[H^{\mathrm{tp}}_{mn}\right]_{\mathrm{dry}}$ and $[H^{\mathrm{cr}}_{mn}]_{\mathrm{dry}}$ represent the compliance contribution matrices of the dry torus and the dry crack, respectively. The compliance contribution matrix for the modified frame (dry torus and saturated crack with a frequency-dependent fluid bulk modulus) is

$$[H_{mn}(\omega)]^{\mathrm{MF}} = \left[H^{\mathrm{tp}}_{mn}\right]_{\mathrm{dry}} + [H^{\mathrm{cr}}_{mn}(\omega)]_{\mathrm{sat}}\,, \tag{9}$$

where the compliance contribution matrix of the torus $\left[H^{\mathrm{tp}}_{mn}\right]_{\mathrm{dry}}$ is frequency-independent but the compliance contribution matrix of the crack $[H^{\mathrm{cr}}_{mn}(\omega)]_{\mathrm{sat}}$ is frequency-dependent. However, the expressions 8 and 9 are accurate only when the torus and the crack are not connected and far from each other, so that there is no elastic interactions. Since we are working with a model where the torus and the crack are interconnected, the expressions 8 and 9 are not valid as illustrated by Alkhimenkov et al. (2020a). The compliance contribution matrix $[H_{mn}(\omega)]^{\mathrm{MF}}$ should be calculated differently, such as in the procedure that we describe below.

Calculation of the model compliance

The overall dispersion and attenuation magnitudes of the modified frame (and hence, of the fully saturated model) are controlled by the elastic bounds: the low-frequency limit — the dry moduli of the model containing the interconnected torus and crack (Figure 5c), and the high-frequency limit — the dry moduli of the model containing the torus while the crack normal compliance is zero (Figure 5b). The corresponding values of the dispersion are illustrated in Figure 6. These low- and high-frequency values can be taken from different sources:

i) These values can be estimated from the laboratory measurements by measuring the low- and high-pressure rock moduli, this procedure is described in many studies, e.g., (Gurevich et al., 2010). We do not examine nor use this approach here.

ii) The second option is to calculate the low- and high-frequency moduli of a dry model numerically.

iii) The third option is to calculate the low- and high-frequency moduli of a dry model analytically.

If the analytical methods are properly used, then the resulting moduli are equivalent to that ones obtained numerically. In this study, we adopt the dry moduli calculated numerically and we provide the workflow to calculate the dry moduli analytically; the numerical and analytical approaches provide us identical results.

One of the most important outcomes of this study is the adequate calculation of the effective elastic moduli of the interconnected pore space using an analytical approach. The pore space consists of two interconnected cavities: the stiff isometric pore (torus) and the compliant crack (flat cylinder). The correct values for the elastic moduli are obtained

numerically for several configurations and shown in Figure 6. Details on the numerical solutions and applied boundary conditions are given in Appendix A. These correct values are used to benchmark the model compliance obtained analytically. The analytical expressions are provided below.

Analytical expressions

To derive the compliance contribution matrix of the interconnected torus and crack $[H_{mn}]_{\text{dry}}$, we employ the conventional approach used in micromechanics to construct the property contribution matrix of complex geometries (e.g., intersecting cracks, inclusions of "irregular" shapes), see chapters 4.3 and 4.4 in Kachanov and Sevostianov (2018). Several different techniques exist, which can be used separately or in combinations. Here, we adopt the following method: by using the results of three-dimensional numerical simulations for the interconnected torus and crack, we find the structure of the compliance contribution matrix, its principal directions and the key geometrical characteristics of inclusions which control the compliance contribution matrix. Then, we construct the compliance contribution matrix of the interconnected torus and crack $[H_{mn}]_{\text{dry}}$ by using the known property contribution tensors for simple geometries (in our case, the crack, the torus and spheroid). It turns out, that all components of the $[H_{mn}]_{\text{dry}}$ are controlled by the torus except for $[H_{33}]_{\text{dry}}$, $[H_{44}]_{\text{dry}}$ and $[H_{55}]_{\text{dry}}$. This is simple to understand because the compliance contribution matrix of the crack is described by the two components only (Schoenberg and Douma, 1988; Schoenberg and Helbig, 1997); thus, the only non-zero components are $[H^{\text{cr}}_{33}]_{\text{dry}}$, $[H^{\text{cr}}_{44}]_{\text{dry}} \equiv [H^{\text{cr}}_{55}]_{\text{dry}}$. However, the crack is connected to the torus, therefore, the theory for cracks embedded into a homogenous material by Schoenberg and Douma (1988); Schoenberg and Helbig (1997) cannot be used here to calculate $[H^{\text{cr}}_{33}]_{\text{dry}}$, $[H^{\text{cr}}_{44}]_{\text{dry}}$, $[H^{\text{cr}}_{55}]_{\text{dry}}$. Instead, from the numerical experiments we find that the $[H_{33}]_{\text{dry}}$, $[H_{44}]_{\text{dry}}$ and $[H_{55}]_{\text{dry}}$ components of the compliance contribution matrix of the interconnected torus and crack are the same as for a spheroid $\left[H^{\text{Ecr}}_{mn}\right]_{\text{dry}}$. From now on, we refer to this spheroid as the extended crack. The shape of the extended crack is such that it works as an envelope for the torus as shown in Figure 7. Thus, we employ $\left[H^{\text{Ecr}}_{33}\right]_{\text{dry}}$, $\left[H^{\text{Ecr}}_{44}\right]_{\text{dry}}$, $\left[H^{\text{Ecr}}_{55}\right]_{\text{dry}}$ components to the contribution matrix of the interconnected torus and crack $[H_{mn}]_{\text{dry}}$. This approach provide us with a very good approximation of the compliance contribution matrix for this particular geometry — the interconnected torus and crack. A detailed workflow is given below (see also Figure 7).

i) The compliance contribution matrix of the dry torus $\left[H^{\text{tp}}_{mn}\right]_{\text{dry}}$ should be calculated

as

$$\left[H_{mn}^{\mathrm{tp}}\right]_{\mathrm{dry}} = \begin{bmatrix} \left[H_{11}^{\mathrm{tp}}\right]_{\mathrm{dry}} & \left[H_{12}^{\mathrm{tp}}\right]_{\mathrm{dry}} & \left[H_{13}^{\mathrm{tp}}\right]_{\mathrm{dry}} & 0 & 0 & 0 \\ \left[H_{21}^{\mathrm{tp}}\right]_{\mathrm{dry}} & \left[H_{22}^{\mathrm{tp}}\right]_{\mathrm{dry}} & \left[H_{23}^{\mathrm{tp}}\right]_{\mathrm{dry}} & 0 & 0 & 0 \\ \left[H_{31}^{\mathrm{tp}}\right]_{\mathrm{dry}} & \left[H_{32}^{\mathrm{tp}}\right]_{\mathrm{dry}} & \left[H_{33}^{\mathrm{tp}}\right]_{\mathrm{dry}} & 0 & 0 & 0 \\ 0 & 0 & 0 & \left[H_{44}^{\mathrm{tp}}\right]_{\mathrm{dry}} & 0 & 0 \\ 0 & 0 & 0 & 0 & \left[H_{55}^{\mathrm{tp}}\right]_{\mathrm{dry}} & 0 \\ 0 & 0 & 0 & 0 & 0 & \left[H_{66}^{\mathrm{tp}}\right]_{\mathrm{dry}} \end{bmatrix}. \tag{10}$$

ii) The compliance contribution matrix of the extended dry crack is calculated $\left[H_{mn}^{\mathrm{Ecr}}\right]_{\mathrm{dry}}$. The diameter of the extended crack is equal to the diameter of the crack ($2b$) plus an extension corresponding to twice the minor diameter of the torus ($4r$), as shown in Figure 7. In other words, the projection of the pore space containing the crack and torus and the projection of the extended crack model onto the $xy-$plane are the same. The thickness of the extended crack is such as the extended crack is a spheroidal envelope for the torus as shown in Figure 7. For our particular geometry, the thickness of the extended crack is approximately twice the minor diameter of the torus, $d_{Mn} = 2r$ (see Figure 7 and Figure 4 for geometrical parameters).

iii) The compliance contribution matrix of the interconnected torus and crack $[H_{mn}]_{\mathrm{dry}}$ is thus constructed by using the obtained components of $\left[H_{mn}^{\mathrm{tp}}\right]_{\mathrm{dry}}$ and $\left[H_{mn}^{\mathrm{Ecr}}\right]_{\mathrm{dry}}$:

$$[H_{mn}]_{\mathrm{dry}} = \begin{bmatrix} \left[H_{11}^{\mathrm{tp}}\right]_{\mathrm{dry}} & \left[H_{12}^{\mathrm{tp}}\right]_{\mathrm{dry}} & \left[H_{13}^{\mathrm{tp}}\right]_{\mathrm{dry}} & 0 & 0 & 0 \\ \left[H_{21}^{\mathrm{tp}}\right]_{\mathrm{dry}} & \left[H_{22}^{\mathrm{tp}}\right]_{\mathrm{dry}} & \left[H_{23}^{\mathrm{tp}}\right]_{\mathrm{dry}} & 0 & 0 & 0 \\ \left[H_{31}^{\mathrm{tp}}\right]_{\mathrm{dry}} & \left[H_{32}^{\mathrm{tp}}\right]_{\mathrm{dry}} & \left[H_{33}^{\mathrm{Ecr}}\right]_{\mathrm{dry}} & 0 & 0 & 0 \\ 0 & 0 & 0 & \left[H_{44}^{\mathrm{Ecr}}\right]_{\mathrm{dry}} & 0 & 0 \\ 0 & 0 & 0 & 0 & \left[H_{55}^{\mathrm{Ecr}}\right]_{\mathrm{dry}} & 0 \\ 0 & 0 & 0 & 0 & 0 & \left[H_{66}^{\mathrm{tp}}\right]_{\mathrm{dry}} \end{bmatrix}. \tag{11}$$

The components $\left[H_{13}^{\mathrm{tp}}\right]_{\mathrm{dry}}$ and $\left[H_{23}^{\mathrm{tp}}\right]_{\mathrm{dry}}$, and corresponding symmetric components, could also be replaced by $\left[H_{13}^{\mathrm{Ecr}}\right]_{\mathrm{dry}}$ and $\left[H_{23}^{\mathrm{Ecr}}\right]_{\mathrm{dry}}$ (which may improve the accuracy) but this effect is of minor importance, thus, we do not explore it in more details. The components $\left[H_{33}^{\mathrm{tp}}\right]_{\mathrm{dry}}$, $\left[H_{44}^{\mathrm{tp}}\right]_{\mathrm{dry}}$ and $\left[H_{55}^{\mathrm{tp}}\right]_{\mathrm{dry}}$ representing the torus are replaced by the components representing the extended crack $\left[H_{33}^{\mathrm{Ecr}}\right]_{\mathrm{dry}}$, $\left[H_{44}^{\mathrm{Ecr}}\right]_{\mathrm{dry}}$ and $\left[H_{55}^{\mathrm{Ecr}}\right]_{\mathrm{dry}}$. The compliance contribution matrices of a torus and extended crack (spheroid) can be calculated analytically as described in chapters 4.3 and 4.2 of Kachanov and Sevostianov (2018) (and references therein).

The compliance contribution matrix of the modified frame is

$$[H_{mn}(\omega)]^{\mathrm{MF}} = \begin{bmatrix} \left[H_{11}^{\mathrm{tp}}\right]_{\mathrm{dry}} & \left[H_{12}^{\mathrm{tp}}\right]_{\mathrm{dry}} & \left[H_{13}^{\mathrm{tp}}\right]_{\mathrm{dry}} & 0 & 0 & 0 \\ \left[H_{21}^{\mathrm{tp}}\right]_{\mathrm{dry}} & \left[H_{22}^{\mathrm{tp}}\right]_{\mathrm{dry}} & \left[H_{23}^{\mathrm{tp}}\right]_{\mathrm{dry}} & 0 & 0 & 0 \\ \left[H_{31}^{\mathrm{tp}}\right]_{\mathrm{dry}} & \left[H_{32}^{\mathrm{tp}}\right]_{\mathrm{dry}} & \left[H_{33}^{\mathrm{Ecr}}(\omega)\right]^{\mathrm{MF}} & 0 & 0 & 0 \\ 0 & 0 & 0 & \left[H_{44}^{\mathrm{Ecr}}\right]_{\mathrm{dry}} & 0 & 0 \\ 0 & 0 & 0 & 0 & \left[H_{55}^{\mathrm{Ecr}}\right]_{\mathrm{dry}} & 0 \\ 0 & 0 & 0 & 0 & 0 & \left[H_{66}^{\mathrm{tp}}\right]_{\mathrm{dry}} \end{bmatrix}. \tag{12}$$

The only difference between the matrices in equation 11 and equation 12 is the component $\left[H_{33}^{\mathrm{Ecr}}(\omega)\right]^{\mathrm{MF}}$. Since the fluid flow takes place in the crack only when the displacement boundary condition in the vertical (z) direction is applied, the component $\left[H_{33}^{\mathrm{Ecr}}(\omega)\right]^{\mathrm{MF}}$ is the only frequency-dependent component. This statement is also supported by the numerical simulations by Alkhimenkov et al. (2020a). The component $\left[H_{13}^{\mathrm{Ecr}}(\omega)\right]^{\mathrm{MF}}$ might also exhibit some dispersion but the magnitude is negligibly small (Alkhimenkov et al., 2020a). The limits of $\left[H_{33}^{\mathrm{Ecr}}(\omega)\right]^{\mathrm{MF}}$ are

$$\lim_{\omega \to +\infty} \left[H_{33}^{\mathrm{Ecr}}(\omega)\right]^{\mathrm{MF}} = \left[H_{33}^{\mathrm{tp}}\right]_{\mathrm{dry}}, \tag{13}$$

and

$$\lim_{\omega \to +0} \left[H_{33}^{\mathrm{Ecr}}(\omega)\right]^{\mathrm{MF}} = \left[H_{33}^{\mathrm{Ecr}}\right]_{\mathrm{dry}}. \tag{14}$$

To separate the contribution of the torus, which is a constant value across a full frequency band, from the contribution of the extended crack compliance, which is frequency dependent, we introduce

$$\left[H_{mn}^{'}(\omega)\right]^{\mathrm{MF}} = [H_{mn}(\omega)]^{\mathrm{MF}} - \left[H_{mn}^{\mathrm{tp}}\right]_{\mathrm{dry}} = \begin{bmatrix} 0 & 0 & 0 & 0 & 0 & 0 \\ 0 & 0 & 0 & 0 & 0 & 0 \\ 0 & 0 & \left[H_{33}^{'}(\omega)\right]^{\mathrm{MF}} & 0 & 0 & 0 \\ 0 & 0 & 0 & \left[H_{44}^{'}\right]_{\mathrm{dry}}^{\mathrm{MF}} & 0 & 0 \\ 0 & 0 & 0 & 0 & \left[H_{55}^{'}\right]_{\mathrm{dry}}^{\mathrm{MF}} & 0 \\ 0 & 0 & 0 & 0 & 0 & 0 \end{bmatrix}. \tag{15}$$

Expression 15 has the same structure as the compliance contribution matrix of a crack written in terms of normal and tangential compliances Z_n and Z_t. The limits of $\left[H_{33}^{'}(\omega)\right]^{\mathrm{MF}}$ are

$$\lim_{\omega \to +\infty} \left[H_{33}^{'}(\omega)\right]^{\mathrm{MF}} = 0, \tag{16}$$

and

$$\lim_{\omega \to +0} \left[H_{33}^{'}(\omega)\right]^{\mathrm{MF}} = \left[H_{33}^{\mathrm{Ecr}}\right]_{\mathrm{dry}} - \left[H_{33}^{\mathrm{tp}}\right]_{\mathrm{dry}} \equiv Z_n^{\mathrm{ap}}, \tag{17}$$

where for simplicity we introduce the apparent normal crack compliance Z_n^{ap}. The apparent tangential crack compliance is $Z_t^{\mathrm{ap}} = \left[H_{44}^{'}\right]_{\mathrm{dry}}^{\mathrm{MF}} \equiv \left[H_{55}^{'}\right]_{\mathrm{dry}}^{\mathrm{MF}}$. Even though the structure of the matrices is the same, the absolute values of the components in equation 15 are calculated differently from the formulas for Z_n and Z_t suggested for cracks embedded into a homogeneous material by Schoenberg and Douma (1988); Schoenberg and Helbig (1997). The effective compliance matrix for the modified frame can be calculated using the equation 7 as

$$[S_{mn}^{*}(\omega)]^{\mathrm{MF}} = S_{mn}^{\mathrm{g}} + \left[H_{mn}^{\mathrm{tp}}\right]_{\mathrm{dry}} + \left[H_{mn}^{'}(\omega)\right]^{\mathrm{MF}}. \tag{18}$$

Finally, the effective compliance moduli of a fully saturated model $[S_{mn}^{*}(\omega)]$ can be obtained by saturating the modified frame $[S_{mn}^{*}(\omega)]^{\mathrm{MF}}$ with a fluid using Gassmann's equations. The expression 18 is the main result of this study and is valid for any geometry of the pore space if the appropriate compliance contribution matrices are used.

Calculation of the frequency-dependent crack stiffness

To derive the frequency-dependent component of the contribution matrix $\left[H_{33}^{'}(\omega)\right]^{\mathrm{MF}}$ (i.e. the normal crack compliance), we note that the thin crack is adequately described by two parameters (as in equation 15), then we use anisotropic Gassmann's equations to calculate the moduli considering the crack saturated. The derivation is simple, requires only algebraic manipulations which are cumbersome, thus we refer to the supplementary material for the full derivation (Maple script). The resulting expression is

$$\left[H_{33}^{'}(\omega)\right]^{\mathrm{MF}} = \frac{(K_g - K_f^{*}(\omega))\,\phi_c\, Z_n^{\mathrm{ap}}}{(K_g - K_f^{*}(\omega))\,\phi_c + K_f^{*}(\omega)\,K_g\, Z_n^{\mathrm{ap}}}, \tag{19}$$

where ϕ_c is the compliant porosity (crack porosity), Z_n^{ap} is the normal apparent compliance of the crack (see expression 17) and K_g is the bulk modulus of the solid grains. If a crack cannot be described by two parameters (for example, the $\left[H_{13}^{'}\right]_{\mathrm{dry}}^{\mathrm{MF}}$ component is also affected), then one can use our Maple script (supplementary material) with already derived equations for the general (anisotropic) form of the solid background and the property contribution matrix of the inclusion, e.g., crack. The expression for the frequency-dependent bulk modulus of the fluid $K_f^{*}(\omega)$ will be given below.

Extension for cracks with finite thickness

If the crack thickness is not so small, so that the aspect ratio is larger than 0.0025 then the limit given in 16 is not equal to zero. A small non-zero value $[Z_n^{\mathrm{ap}}]^{\mathrm{fth}}$ will be present,

$$\lim_{\omega \to +\infty} \left[H_{33}^{'}(\omega)\right]^{\mathrm{MF}} = [Z_n^{\mathrm{ap}}]^{\mathrm{fth}} \tag{20}$$

and the normal apparent crack compliance becomes

$$[Z_n^{\mathrm{ap}}]^{\mathrm{f}} = Z_n^{\mathrm{ap}} - [Z_n^{\mathrm{ap}}]^{\mathrm{fth}} \tag{21}$$

In this case, the only modification that is needed is a slight change in expression 19 by including the additional compliance $[Z_n^{\mathrm{ap}}]^{\mathrm{fth}}$

$$\left[H_{33}^{'}\right]^{\mathrm{MF}} = \frac{(K_g - K_f^*(\omega))\,\phi_c\;[Z_n^{\mathrm{ap}}]^{\mathrm{f}}}{(K_g - K_f^*(\omega))\,\phi_c + K_f^*(\omega)\,K_g\;[Z_n^{\mathrm{ap}}]^{\mathrm{f}}} + [Z_n^{\mathrm{ap}}]^{\mathrm{fth}}\,. \tag{22}$$

Relaxation of the crack stiffness

In the analytical model, the relaxation of the crack stiffness due to fluid pressure diffusion controls the frequency-dependence of the effective elastic moduli of the medium. The relaxation of the crack stiffness can be modeled via the the relaxation of the fluid bulk modulus $K_f^*(\omega)$ in the crack. In several previous studies, the task is reduced to solving the problem for a crack only by applying boundary conditions directly to the crack walls and to the tip of the crack (e.g., Murphy et al. (1986)). Then, the derived expression for $K_f^*(\omega)$ is treated as the crack stiffness. Unfortunately, applying boundary conditions to the crack walls and to the crack tip produces a different result compared to applying the boundary conditions directly to the walls of the model. For illustration, we show the models considering zero fluid pressure at the crack tip and the Big pore model, with the corresponding results of numerical simulations (Figure 8).

In the rock physics literature, the relaxation of fluid pressure was derived by solving an equation for fluid pressure distribution p in the the flat cylinder (crack) under sinusoidal loading $\Delta h e^{i\omega t}$ applied to the walls of the crack, Δh is the displacement of the crack walls (e.g., Murphy et al. (1986); Dvorkin and Nur (1993)). Then, by integrating the fluid pressure p over the thickness and area of the crack, the frequency-dependent fluid bulk modulus $K_f^*(\omega)$ was determined. In the mechanics literature, similar problems were solved in time domain for different visco-elastic materials (e.g., Chalhoub and Kelly (1990); Tsai and Lee (1998)). All the solutions are very similar for the same geometries and applied boundary conditions with slight differences depending on the approximations done during the derivation.

We use symbolic environment Maple to derive a general structure of the solutions for the frequency-dependent fluid bulk modulus $K_f^*(\omega)$. We start with the known approach by applying the boundary conditions to the walls of the crack (Murphy et al., 1986; Tsai and Lee, 1998). But afterwards we modify the resulting solution by taking into account the heterogeneous stress field induced by the torus. In Cartesian coordinates, the expression for fluid pressure under the compression strain ϵ_c applied to the walls of the crack is

$$\frac{\partial^2 p}{\partial x^2} + \frac{\partial^2 p}{\partial y^2} - k^2\, p = -k^2\, K_f \epsilon_c, \tag{23}$$

where k is a parameter a function of the applied strain and rheology of the crack (e.g., Tsai and Lee (1998)). In polar coordinates, the expression for fluid pressure becomes

$$\frac{\partial^2 p}{\partial r^2} + \frac{1}{r}\frac{\partial p}{\partial r} - k^2\, p = -k^2\, K_f \epsilon_c \tag{24}$$

The stiffness of the crack H can be expressed via the surface integral over the crack area S for the averaged vertical stress $\bar{\sigma}_{zz}$,

$$H = -\left[\int_S \bar{\sigma}_{zz}\, dS\right] / (S\epsilon_c), \quad \bar{\sigma}_{zz} = \left[\int_h \sigma_{zz}\, dh\right] / h. \tag{25}$$

If the crack rheology represents a pure fluid, then $H \equiv K_f$. Similar equations were considered in the previous studies by Murphy et al. (1986); Chalhoub and Kelly (1990).

Zero fluid pressure at the crack tip

In the modified frame configuration, the crack is connected to the dry isometric pore, which corresponds to zero fluid pressure boundary condition at the edge of the crack. This configuration was studied by Chalhoub and Kelly (1990); Tsai and Lee (1998). The solution for $K_f^*(\omega)$ treating the crack as a flat cylinder is

$$K_f^*(\omega) = K_f + \frac{4}{3}i\omega\eta - \frac{\left(K_f - \frac{2}{5}i\omega\eta\right)^2}{\left(K_f + \frac{4}{3}i\omega\eta\right)\frac{\bar{k}_1\, J_0(\bar{k}_1)}{J_1(\bar{k}_1)} - i\omega\eta}, \tag{26}$$

where η is a fluid dynamic viscosity, J_0 and J_1 are the are the Bessel functions of the first kind of order 0 and 1, respectively, and $\bar{k}_1$ is defined as

$$\bar{k}_1 = \frac{1}{\alpha}\sqrt{3i\omega\eta/(K_f + \frac{4}{3}i\omega\eta)}, \tag{27}$$

where $\alpha = h/(2b)$ is the crack aspect ratio. A different expression for $K_f^*(\omega)$ was provided by Chalhoub and Kelly (1990)

$$K_f^*(\omega) = K_f\left[1 - \frac{2\, J_1(\bar{k}_2)}{\bar{k}_2\, J_0(\bar{k}_2)}\right], \tag{28}$$

where $\bar{k}_2$ is

$$\bar{k}_2 = \frac{1}{\alpha}\sqrt{-3i\omega\eta/K_f}. \tag{29}$$

It was pointed out by Tsai and Lee (1998) that the solution 28 is similar to 26 for Poisson ratio = 0.5 but different if Poisson ratio $\leq$ 0.5 (the solution 26 matches numerical solutions for Poisson ratio $\leq$ 0.5). Thus, for fluids (Poisson ratio = 0.5) either solution 26 or 28 can be used (Figure 9). The expression 28 was used by Gurevich et al. (2010); Collet and Gurevich (2016) for the relaxation of the fluid bulk modulus of the modified frame.

Non-zero fluid pressure at the crack tip

In this configuration, the crack is connected to the saturated isometric pore meaning that the fluid pressure in such a pore will increase due to the fluid flow from the crack (see Murphy et al. (1986) for the precise boundary conditions). In this case, during the relaxation of the fluid bulk modulus, the fluid "feels" the finite volume of the isometric pore. The solution of 25 for this boundary condition is (Murphy et al., 1986)

$$K_f^*(\omega) = K_f\left[1 - \frac{2\, V_{por}\, J_1(\bar{k}_2)}{2\, V_{cr} J_1(\bar{k}_2) + \bar{k}_3\, V_{por}\, J_0(\bar{k}_2)}\right] \tag{30}$$

V_{por} is the volume of the stiff pore and $V_{cr} = \pi h b^2$ is the volume of the compliant crack. The geometrical parameters h, b and r are given in Table 1. For a torus, V_{por} is calculated

as $V_{por} = 2\pi^2(b+r)r^2$. Under the assumption of $V_{por} \to \infty$, the expression 30 reduces to expression 28 (it can be seen from expression 30 by removing terms with $1/V_{por}$). The low-frequency limit of K_f^* calculated using equation 30 is

$$\lim_{\omega \to 0} K_f^* = \frac{V_{cr} K_f}{V_{cr} + V_{por}}. \tag{31}$$

Note, that the shape of the curves in expressions 26, 28 and 30 is the same (Figure 9a), which means that for the Big pore model solutions 26, 28 and 30 are equivalent. In other words, the volume of the Big pore is so large compare to the volume of the crack, that zero fluid pressure boundary condition provides us a good approximation. The low-frequency limit $K_f^* \neq 0$ (but close to 0) in equation 30 compared to expressions for zero fluid pressure boundary condition at the edge of the crack (expressions 26, 28 where $K_f^* = 0$). The high-frequency limit of the K_f^* is

$$\lim_{\omega \to \infty} K_f^* = \left(1 + 2\left(\frac{\cos(ka + \pi/4)}{\sin(ka + \pi/4)}\right)\frac{1}{ka}\right) K_f. \tag{32}$$

This high-frequency limit (Eq. 32) also applies to expression 28 for $K_f^*(\omega)$.

Modification of the relaxation of the fluid bulk modulus for the classical geometry

Alkhimenkov et al. (2020a) showed that the $[C_{33}^*(\omega)]_{\text{sat}}$ component obtained via the analytical model by using $K_f^*(\omega)$ (Eq. 28) is in agreement with the numerical simulation for zero fluid pressure at the crack tip and no stiff pore (Figure 8). It means that if the background material is homogeneous, the relaxation of the fluid bulk modulus is not affected (or the effect is negligible) by the surrounding homogeneous grains. In other words, applying boundary conditions to the walls of the crack or to the walls of the model produces similar results in this special case of no stiff pore (Figure 8ab). But this configuration is not realistic. For a more realistic scenario, when a stiff pore is present (Figure 8c), the $[C_{33}^*(\omega)]_{\text{sat}}$ component obtained via the analytical model by using $K_f^*(\omega)$ obtained analytically for the configuration shown in Figure 8a diverges from the numerical result (Alkhimenkov et al., 2020a). This disagreement is due to the presence of the isometric pore connected to the crack, which changes the stress field in the model. Because of the modified stress field, the fluid flow is also affected and the boundary conditions applied to the wall of the crack are no longer accurate (Figure 8cd). According to numerical solutions for the models where a torus is connected to a crack, the high-frequency slopes of the dispersion and attenuation curves are substantially different from those obtained via solution for the crack only having a zero fluid pressure boundary condition at the tip (Eq. 28) (Figure 8e). A similar observation has been pointed out by Solazzi et al. (2021) for partially saturated cracks.

By analyzing the numerical results, we find that the $1/Q$ at high-frequencies is proportional to $\approx \omega^{-1/2}$ for the classical geometry (the crack connected to the toroidal pore). However, the solutions for $K_f^*(\omega)$ (expressions 26, 28 and 30) and the resulting $1/Q$ exhibit

different behavior at high-frequencies compare to the numerical solutions. Therefore, we derive an approximation to the relaxation of the fluid bulk modulus $K_f^*(\omega)$ for the classical geometry by simply using the solution 30 with a modified high-frequency asymptote. For that, we use a special form of a branching function. The concept of a branching function is simple and allows us to find an accurate approximation for a given cumbersome exact solution (Pride et al., 1993; Johnson, 2001). A branching function is designed such that it satisfies the Kramers–Kronig relations, thus can be used to approximate seismic attenuation and dispersion curves. To construct the branching function, one needs to know the low- and high-frequency limits along with the low- and high-frequency asymptotes of the exact solution. We use the following branching function,

$$K_f^*(\omega) = K_f - (K_f - y \cdot K_f^{LF})/(1 - \zeta + \zeta\sqrt{1 + i\omega\tau/\zeta^2}), \tag{33}$$

where $y = 0$ for the solution considering zero fluid pressure at the crack tip or $y = 1$ for the solution considering non-zero fluid pressure boundary condition at the crack tip. In equation 33, K_f corresponds to the high frequency limit of the exact solution (which is exactly the fluid bulk modulus), K_f^{LF} (if $y = 1$) or 0 (if $y = 0$) correspond to the low frequency limit of the exact solution 30 or 26, respectively. The two parameters ζ and τ control the shape of the branching function. The recipe to construct the branching function is the following:

i) We extract several parameters of the solution 30 for $K_f^*(\omega)$: the low- and high-frequency limits of $K_f^*(\omega)$, the low-frequency asymptote of $1/Q_{K_f^*} = \text{Im}\left(K_f^*(\omega)\right)/\text{Re}\left(K_f^*(\omega)\right)$ and the characteristic frequency f_c^{crack} of $1/Q_{K_f^*}$ (at the maximum of $1/Q_{K_f^*}$). This gives us four parameters.

ii) We construct the branching function 33 with $y = 1$ to approximate the solution 30 using the known parameters obtained in i) but with the modified high-frequency asymptote being proportional to $\approx \omega^{-1/2}$. There are only four parameters in the branching function 33. The last relation to close the system of equations is that the intersection of low- and high-frequency asymptotes of the branching function coincides with the characteristic frequency f_c^{crack} obtained in i). The resulting modified solution is shown in Figure 9 (black squares).

iii) The final modified solution for $K_f^*(\omega)$ is obtained from the step ii) by setting $y = 0$ in the expression 33. This step is needed to obtain the solution for the zero fluid pressure boundary condition at the crack tip since our analytical model is based on the modified frame (Figure 3).

The calculations in steps i), ii) and iii) are simple, require only algebraic manipulations but they are cumbersome, thus we refer to the supplementary material for the full derivation (Maple script). The resulting expressions for the branching function are given below.

By setting $y = 0$ in expression 33 (corresponding to zero fluid pressure at the crack tip), the frequency-dependent bulk modulus of the fluid $K_f^*(\omega)$ becomes

$$K_f^*(\omega) = K_f - K_f/(1 - \zeta + \zeta\sqrt{1 + i\omega\tau/\zeta^2}), \tag{34}$$

where the parameter τ is calculated as

$$\tau = \frac{3}{4}\frac{\eta}{K_f}\frac{\zeta}{\alpha^2}, \tag{35}$$

and the parameter ζ is calculated as

$$\zeta = \frac{128}{27}\frac{K_f}{\eta^3}\frac{(K_f^{LF})^2}{(f_c^{crack})^3}\alpha^6, \tag{36}$$

with f_c^{crack} given by

$$f_c^{crack} = \frac{4}{\sqrt{3}}\frac{\sqrt{K_f \cdot K_f^{LF}}}{\eta}\alpha^2. \tag{37}$$

The parameter f_c^{crack} determines the characteristic frequency of $K_f^*(\omega)$. The apparent fluid bulk modulus at low frequencies K_f^{LF} is

$$K_f^{LF} = \frac{V_{cr}K_f}{V_{cr} + V_{por}}, \tag{38}$$

The low-frequency asymptote of the K_f^* calculated using equation 33 is

$$\lim_{\omega\to 0} K_f^* = \frac{(K_f - K_f^{LF})\tau}{K_f^{LF}\zeta}\omega. \tag{39}$$

The high-frequency asymptote of the K_f^* calculated using equation 33 is

$$\lim_{\omega\to \infty} K_f^* = \frac{(K_f - K_f^{LF})\sqrt{2}}{2K_f\sqrt{\tau}}\frac{1}{\omega^2}. \tag{40}$$

It is possible that for some specific parameters that expressions 34-38 lose their accuracy. In this case, one can modify the expressions 34-38 using the Maple symbolic environment to improve the accuracy. We do not explore in detail the accuracy of the boundary conditions for the crack tip proposed by Murphy et al. (1986) (the solution 30), different boundary conditions may slightly modify the expression 30 and the derived modification of this solution 34-38.

Note that the branching function of the form 33 was used to approximate cumbersome exact solutions in different contexts by many authors (Pride et al., 1993; Johnson, 2001). Note that 33 is designed to approximate solutions in the stiffness. A similar branching functions exists to approximate solutions in the compliance, which is more suitable for some applications (Gurevich et al., 2009).

Big pore model

Figure 9 shows the real part of the frequency-dependent fluid bulk modulus K_f^* and the dimensionless attenuation calculated using different expressions for the Big pore model

with $\alpha = 0.005$. Since the volume of the big pore is large, the expressions for K_f^* 26 and 28 reduce to expression 30. Note, that $1/Q$ of K_f^* of Eq. 26 and 28 is the same as for 30 for frequencies larger than the characteristic frequency but tend to infinity for frequencies lower than the characteristic frequency because $K_f^* \to 0$ as $\omega \to 0$. K_f^* calculated via the branching function 33 ($y = 1$) is identical to 30 except for the high frequency asymptote. Note, that asymptotes of the branching function intersect at the characteristic frequency of K_f^* calculated via equation 30.

Figure 10 is similar to Figure 9 but K_f^* calculated via the equation 34 is shown together with the numerical solution. The numerical solution was obtained from the simulations for the modified frame of the Big pore model ($\alpha = 0.005$), and then inverting for K_f^* via the analytical formulas 18 and 19. K_f^* calculated via equation 34 is in agreement with the numerical solution (note, that there are no fitting parameters in equation 34).

Small pore model

Figure 11 shows the real part of the frequency-dependent fluid bulk modulus K_f^* and the dimensionless attenuation calculated using different formulas for the Small pore model with $\alpha = 0.0025$. The branching function with $y = 0$ (equation 33 or, equivalent, equation 34) corresponds to the configuration with zero fluid pressure at crack tip (which is used in the present analytical model for the modified frame). At low frequencies, K_f^* calculated via the branching function 33 ($y = 0$) and the solution 30 are not equal to zero because the volume of the Small pore is only slightly larger than the volume of the crack. $1/Q$ calculated via the the branching with $y = 0$ (equation 33 or equation 34) is in agreement with the numerical solution.

Summary

Our analytical model requires (i) the calculation of the effective compliance matrix of the modified frame (expression 18), (ii) the calculation of the frequency dependent component $\left[H_{33}^{'}\right]^{\mathrm{MF}}$ (expression 19), which represents the frequency-dependent crack stiffness, (iii) the calculation of the effective stiffness moduli of a fully saturated model by applying Gassmann's equations (Gassmann, 1951). If the low- and high-frequency limits of the dry model are known, then the step (i) can be skipped; the frequency dependent component $\left[H_{33}^{'}\right]^{\mathrm{MF}}$ (expression 19) provides the transition from low- to high-frequencies (step (ii)).

(i) The modified frame

Our analytical model requires the calculation of effective compliance matrix of the modified frame (expression 18),

$$[S^*_{mn}(\omega)]^{\mathrm{MF}} = S^{\mathrm{g}}_{mn} + \left[H^{\mathrm{tp}}_{mn}\right]_{\mathrm{dry}} + \left[H^{'}_{mn}(\omega)\right]^{\mathrm{MF}}, \tag{41}$$

where S^{g}_{mn} is the compliance matrix of the solid grain material, $\left[H^{\mathrm{tp}}_{mn}\right]_{\mathrm{dry}}$ is the compliance contribution matrix of the isometric pore (torus) and $\left[H^{'}_{mn}(\omega)\right]^{\mathrm{MF}}$ is the additional compliance contribution matrix of the crack connected to the torus. The compliance contribution matrices of a torus $\left[H^{\mathrm{tp}}_{mn}\right]_{\mathrm{dry}}$ and extended crack (ellipsoid) $\left[H^{\mathrm{Ecr}}_{mn}\right]_{\mathrm{dry}}$ can be calculated analytically using expressions from e.g., Kachanov and Sevostianov (2018). Then, following the workflow presented in Figure 7, the $\left[H^{'}_{mn}(\omega)\right]^{\mathrm{MF}}$ can be calculated as $\left[H^{'}_{mn}(\omega)\right]^{\mathrm{MF}} = [H_{mn}(\omega)]^{\mathrm{MF}} - \left[H^{\mathrm{tp}}_{mn}\right]_{\mathrm{dry}}$ (see formula 15 for details), where $[H_{mn}(\omega)]^{\mathrm{MF}}$ is constructed by expression 12 using the already obtained $\left[H^{\mathrm{tp}}_{mn}\right]_{\mathrm{dry}}$ and $\left[H^{\mathrm{Ecr}}_{mn}\right]_{\mathrm{dry}}$.

(ii) The frequency-dependent crack stiffness

The $\left[H^{'}_{33}\right]^{\mathrm{MF}}$ component is calculated by

$$\left[H^{'}_{33}(\omega)\right]^{\mathrm{MF}} = \frac{(K_g - K^*_f(\omega))\,\phi_c\,Z^{\mathrm{ap}}_n}{(K_g - K^*_f(\omega))\,\phi_c + K^*_f(\omega)\,K_g\,Z^{\mathrm{ap}}_n}, \tag{42}$$

where ϕ_c is the compliant porosity (crack porosity), Z^{ap}_n is the apparent normal compliance of the crack (see expression 17) and K_g is the bulk modulus of the solid grains. The expression for the frequency-dependent bulk modulus of the fluid $K^*_f(\omega)$ can be calculated by using equation 34. For cracks of finite thickness, equation 22 should be used instead of equation 42.

(iii) The moduli of a fully saturated model

Finally, the effective stiffness moduli of a fully saturated model $[C^*_{mn}(\omega)]_{\mathrm{sat}}$ can be obtained by using anisotropic Gassmann's equations (Gassmann, 1951) at each frequency to $[S^*_{mn}(\omega)]^{\mathrm{MF}}$:

$$[C^*_{mn}(\omega)]_{\mathrm{sat}} = \left([S^*_{mn}(\omega)]^{\mathrm{MF}}\right)^{-1} + \alpha_m \alpha_n M, \tag{43}$$

$$\alpha_m = 1 - \left(\sum_{n=1}^{3} C^{\mathrm{MF}}_{mn}\right) / K_g / 3, \tag{44}$$

for $m = 1, 2, 3$ and $\alpha_4 = \alpha_5 = \alpha_6 = 0$, and where

$$M = \left(\phi/K_f + (1-\phi)/K_g - K^*/K_g^2\right)^{-1}, \tag{45}$$

$$K^* = \frac{1}{9}\sum_{m=1}^{3}\sum_{n=1}^{3} C_{mn}^{\mathrm{MF}}(\omega), \tag{46}$$

where ϕ is the total porosity of the medium without the compliant porosity (which is neglected because the compliant porosity is usually two or more orders of magnitude lower than the stiff pore's porosity), K^* is the generalized bulk modulus of the modified frame and α_m is the Biot-Willis coefficient.

VALIDATION AGAINST THREE-DIMENSIONAL NUMERICAL SOLUTIONS

For the validation, we consider several 3-D models consisting of a pore space embedded in an elastic solid grain material. The numerical methodology is described in Appendix A and was introduced by Quintal et al. (2016, 2019); the boundary conditions for the direct relaxation tests to compute all components of the stiffness matrix are described in Alkhimenkov et al. (2020a,b). The models considered are the following:

i) The saturated Big pore model with crack aspect ratio $\alpha = 0.0025$. This is the model that was shown in Figure 4.
ii) The saturated Big pore model with finite thickness crack (aspect ratio $\alpha = 0.005$).
iii) The modified frame of the Big pore model with finite thickness crack (aspect ratio $\alpha = 0.005$).
iv) The modified frame of the Small pore model with crack aspect ratio $\alpha = 0.0025$. Here the isometric pore represented by the torus is small.

The geometrical properties of the models with crack aspect ratio $\alpha = 0.0025$ are shown in Table 1 and the material parameters are shown in Table 2. The model geometry is scalable; i.e., if all geometric parameters of the models are divided or multiplied by any number, the results will be the same.

Big pore model

Figure 12 shows results for the $[C^*_{33}]_{\text{sat}}$ complex-valued component of the stiffness matrix obtained using the present analytical model, the model of Collet and Gurevich (2016) with two different sets of normal and tangential compliances (see Appendix B and Alkhimenkov et al. (2020a) for more details) and the numerical solution for the model shown in Figure 4. The model A of Collet and Gurevich (2016) doesn't take into account the connectivity of the crack and pore gives stiffer moduli of the rock at low frequencies compared to the correct moduli. The model B of Collet and Gurevich (2016) takes into account the connectivity of the crack and pore using the modification introduced by Alkhimenkov et al. (2020a) and gives correct moduli of the rock at low frequencies. The aspect ratio is $\alpha = 0.0025$ which corresponds to the limit where the crack aperture is small enough so that at high-frequencies the fluid stiffens the crack to the point that $Z_n^{\text{ap}} = 0$. Our analytical model is in good agreement with the numerical solution. For the big pore model, f_c^{crack} (equation 37) is almost identical to the characteristic frequency f_c of the fully saturated model.

Big pore model with the finite thickness crack

Figure 13 shows results for the $[C_{33}^*]_{\text{sat}}$ complex-valued component of the stiffness matrix obtained from the our analytical model, the models A and B of Collet and Gurevich (2016) and from the numerical simulation. The aspect ratio here is $\alpha = 0.005$. The high frequency limit of the $[C_{33}^*]_{\text{sat}}$ slightly lower due to the increased crack aperture and, thus, compliance. Our present analytical model takes into account the non-zero value of Z_n^{ap} corresponding to larger aspect ratios showing a good agreement with numerical solutions.

Modified frame of the Big pore model with finite thickness crack

We also validate the extension of the analytical model to finite thickness crack against a modified frame configuration. Figure 14 shows results for the $[C_{33}^*]^{\text{MF}}$ complex-valued component of the stiffness matrix obtained from the present analytical model, the models A and B of Collet and Gurevich (2016) and from the numerical simulation. In this case, dispersion and attenuation is much stronger than in Figure 13 because the fluid in the crack can freely flow into the empty pore without experiencing any difficulties due to the finite volume of the torus that would otherwise result in an increase in fluid pressure at low frequencies. Our analytical model is in good agreement with numerical solutions confirming that it can adequately describe the frequency-dependence of the modified frame.

Modified frame of the Small pore model

We also apply our analytical model to a different pore space configuration — Small pore model (Table 1). In this configuration, the volume of the torus is small, thus dispersion and attenuation are also small. But the modified frame of the Small pore model shows significant dispersion and attenuation (Figure 15). We consider an aspect ratio $\alpha = 0.0025$. The result from pur analytical model is in a good agreement with the numerical solutions.

DISCUSSION

The key features making our model accurate

There are two key features which make the present analytical model very accurate. The first one is the correct calculation of the model compliances. We provide the workflow to obtain the effective compliance matrix which takes into account the connectivity of the stiff pore and the compliant crack; it provides the correct values of the low and high frequency limits of the stiffness moduli. The second feature is the accurate description of the relaxation of the compliant crack due to fluid pressure diffusion; it gives the correct shape of the dispersion and attenuation curves across the whole frequency range.

The usual treatment of the pore and crack as being disconnected when calculating the model compliance provides inaccurate predictions of the overall attenuation and dispersion. The error of the low frequency limit of the dispersion curve can be as large as 100% of the crack compliance, as it can be seen in Figure 12 (blue curve, analytical model A of Collet and Gurevich (2016)). However, once the workflow for calculating the model compliance takes into account the connectivity of the pore and crack, the low and high frequency limits of the dispersion curve become accurate (green curve, modification of analytical model of Collet and Gurevich (2016)). The modification of the analytical model of Collet and Gurevich (2016) (model B) was provided by Alkhimenkov et al. (2020a)(Appendix B). Our analytical model is based on the property contribution tensors which provides a general approach for calculating the moduli and can be extended for more complex geometries of the pore space (equation 41). The presented workflow (Figure 7) to construct the property contribution tensor of the interconnected pore and crack provides the correct values of the low and high frequency limits of the dispersion curve (Figures 12-15).

Small deformations caused by the wave propagation compress the compliant crack and cause fluid pressure diffusion or squirt flow. The fluid pressure distribution in the crack is significantly affected by the inhomogeneous stress field introduced by the isometric pore (especially at frequencies higher than the characteristic frequency). The stiffening effect of the fluid in the crack is substantially different for homogeneous and heterogeneous stress field distributions surrounding the crack (see Figure 8). Thus, we had to modify the expression for the relaxation of the crack stiffness for this specific geometry of the pore space represented by the interconnected torus and crack. This modification depends on the shape of the pore space and is explored in more details in Part 2 of this study. The popular idea of considering certain viscoelastic moduli describing the stiffening effect of fluid is, in general, imprecise. The stiffness of the fluid can be replaced by viscoelastic moduli only for particular pore space geometries, as we show in the present and follow up studies.

The effect of the finite volume of the stiff pore

The volume of the isometric (stiff) pore V_{por} has a key influence on the magnitude of the dispersion and attention. If this volume is significantly larger than the volume of a compliant crack V_{cr} (i.e. by two orders of magnitude or more), then the fluid in the crack does not "feel" that the volume of the isometric pore is finite. In other words, in the low-frequency limit the normal crack compliance of the saturated model is the same as if it was dry. This can be seen in Figure 10, where in the low frequency limit K_f^* approaches zero.

On the other hand, if the volume of an isometric pore is similar to the volume of a compliant crack (or just an order of magnitude larger), then the fluid in the crack does "feel" that the volume of the isometric pore is finite and the resulting dispersion and attenuation are reduced. At low-frequencies fluid flow from the crack into the isometric pore significantly increases fluid pressure in the stiff pore. As a result, in the low-frequency limit the normal crack compliance has a finite non-zero value. This can be seen in Figure 11 (Small pore model) where in the low frequency limit K_f^* approaches ≈ 0.6 GPa. The resulting attenuation and dispersion are very small (Alkhimenkov et al., 2020a).

The expression 31 gives an estimate of $K_f^*(\omega)$ for the case where the fluid flow in the crack "feels" the finite volume of the isometric pore, the low frequency limit of $K_f^*(\omega)$ is

$$K_f^{LF} = \frac{V_{cr} K_f}{V_{cr} + V_{por}}. \tag{47}$$

The resulting value of K_f^{LF} can be used in expression 19 to calculate the normal fracture compliance

$$Z_n^{\mathrm{LF}} = \frac{(K_g - K_f^{LF})\,\phi_c\, Z_n^{\mathrm{ap}}}{(K_g - K_f^{LF})\,\phi_c + K_f^{LF}\, K_g\, Z_n^{\mathrm{ap}}}, \tag{48}$$

The value Z_n^{LF} gives the quantitative answer to the question: "how strong will be the stiffening effect of the crack at low frequencies?"

The importance of pore connectivity and elastic interactions

Elastic interaction is a very popular topic in mechanics as well as in rock physics. When the concentration of cracks or pores is small, the elastic interactions are also small and can be ignored. In this case, for calculating the effective elastic moduli one can use methods which do not take into account elastic interactions (so-called non-interactive approximation of effective medium theory); these methods usually provide exact results for simple pore geometries. When the concentration of cracks or pores is increased, the elastic interactions take place and affect the effective elastic properties. Exact results are possible only for a limited number of configurations, usually for two-body problems. For many-body problems many approximations exist. The effect of pore connectivity, however, is a distinct subject with a distinct contribution.

Figure 16 shows a slice equivalent to that in Figure 4 with the three pore configurations: the torus and the crack are connected, the torus and the crack are disconnected but close to each other, and the torus and the crack are disconnected and a bit further from each other. On top of each subplot, the effective stiffness component $[C^*_{33}]_{\rm dry}$ calculated numerically (with properties given in Tables 1 and 2) is shown. Roughly, the pore is reducing the $[C^*_{33}]_{\rm dry}$ component of the solid grain material by 10.6 GPa (from 94.6 GPa to 84 GPa) (Figure 6). Then, embedding the crack connected to the pore is further reducing the $[C^*_{33}]_{\rm dry}$ component by 22.5 GPa (from 84 GPa to 61.5 GPa). Conversely, if the crack is not connected to the pore, the reduction of the $[C^*_{33}]_{\rm dry}$ component is only 11 GPa (from 84 GPa to 73 GPa), thus the "connectivity" costs 11.5 GPa. The "connectivity" cost to the stiffness of the model (11.5 GPa) is five times bigger than the effect of elastic interactions (2 GPa) shown in Figure 16. This example shows that the first order effect to the effective elastic properties is due to the connectivity of the pores and cracks. The effect of elastic interactions on the effective elastic properties is of secondary importance and can be considered only when interconnectivity is taken into account. Roughly, interconnectivity significantly increases the "apparent" crack density in such a way that the surface of the crack together with its invisible continuation into the isometric pore control the effective elastic properties. Such "apparent" crack density can be two or even more times bigger than the crack density of the cracks only. Unfortunately, elastic interactions are very popular in research articles but interconnectivity is usually ignored.

The correctness of expression 19 for the normal crack compliance

The expression 19 is equivalent to the expression derived before (e.g., Gurevich (2003)):

$$Z_n^{\rm sat} = \frac{Z_n}{1 + \frac{Z_n}{\phi_c(1/K_f - 1/K_g)}}, \tag{49}$$

where $Z_n^{\rm sat}$ is the normal crack compliance of the saturated crack, K_f can be replaced by $K_f^*(\omega)$ (e.g., Collet and Gurevich (2016)). The expression 19 (or 49) is exact for the following configuration: a thin crack embedded into a solid grain material; the crack compliance is described by the only two parameters Z_n and Z_t. Then, we apply anisotropic Gassmann's equation to calculate the moduli considering the crack saturated. The result of Gassmann's equations is the only modification of Z_n, which becomes $Z_n^{\rm sat}$.

In the present framework, we use Gassmann's equations in two ways. First, we use them to saturate the crack while the stiff pore remains dry. This violates the assumptions for the applicability of Gassmann's equations (because the model is three-phase: grains, dry stiff pore and crack saturated with a fluid). Second, we apply Gassmann's equations to the modified frame to calculate the moduli of the fully saturated model. Since the modified frame is heterogeneous, this also violates the assumptions for the applicability of Gassmann's equations. However, numerical solutions show that the present analytical model is very accurate for the modified frame as well as for the fully saturated pore space.

One explanation for such accuracy is that the pore space is correctly partitioned into the stiff pore and compliant crack. The stiff pore acts as a "storage" volume for the fluid and doesn't contribute directly to the overall attenuation; the fluid pressure is approximately uniform at each frequency. The fluid flow in the compliant crack is responsible for the overall attenuation of the model.

In the low-frequency limit, the expression 19 gives the normal crack compliance $Z_n^{\rm ap}$ of the dry crack. In this case, we apply anisotropic Gassmann's equations to saturate the model where the pore and the crack are present; this procedure is correct without regard to the pore space structure. If in the anisotropic Gassmann's equations we use the whole porosity (stiff pore and crack porosities), then the result is exact in the low-frequency limit.

The choice of the model

Figure 17 shows the Big torus model with the crack aperture h on the left and the crack aperture $50h$ on the right. Surprisingly, the $[C_{33}^*]_{\rm dry}$ component of the effective elastic moduli of the dry model is the same for both models. This means that the torus surrounding cracks controls the stiffness because it is connected to the whole circumference of the crack. The components of the stiffness matrix $[H_{33}]_{\rm dry}$, $[H_{44}]_{\rm dry}$ and $[H_{55}]_{\rm dry}$ are controlled by the torus only. This geometry cannot represent the rock pore space adequately since cracks do control the stiffness in real rocks. That's why in Part 2 we explore more complex pore space geometries where isometric stiff pores are rather spherical and the crack circumference is only partially connected to stiff pores.

A standard linear solid as an analytical model

The standard linear solid (SLS) rheology for the $[C_{33}^*(\omega)]_{\rm sat}$ component can be written as

$$[C_{33}^*(\omega)]_{\rm sat} = \frac{[C_{33}^*]_{\rm sat}^{LF} + i\,[C_{33}^*]_{\rm sat}^{HF}\,(\omega/\omega_c)}{1 + i\,(\omega/\omega_c)}, \tag{50}$$

where $[C_{33}^*]_{\rm sat}^{LF}$ and $[C_{33}^*]_{\rm sat}^{HF}$ are the effective moduli of the saturated model at low- and high-frequency limits, respectively and ω_c is the characteristic frequency (Mavko et al., 2020). Thus, only three input parameters are needed to calculate dispersion and attenuation. Figure 18 shows results for the $[C_{33}^*(\omega)]_{\rm sat}$ complex-valued component of the stiffness matrix obtained with the present analytical model, with the SLS model, with the modified model of Collet and Gurevich (2016) (model B, with correct limits), with the approximation of the modified model of Collet and Gurevich (2016) (model B) and with the numerical solution. Note, that model of Collet and Gurevich (2016) is the same as the model of Gurevich et al. (2010) but for anisotropic media (all cracks with the same orientation). Gurevich et al. (2010) proposed an approximation for the relaxation of the fluid bulk modulus $K_f^*(\omega)$ (Eq. 28),

$$K_f^*(\omega) = -(\bar{k}_2)^2 K_f/8 \tag{51}$$

If this approximation 51 is used for $K_f^*(\omega)$ in the modified model of Collet and Gurevich (2016) (model B), then it becomes identical to the SLS result across all frequencies (Figure 18). In other words, SLS is almost identical to the model of Collet and Gurevich (2016), thus a single expression 50 can be used to obtain the same dispersion and attenuation curves. A similar observation is given in Carcione and Gurevich (2011) for an isotropic squirt flow model of Gurevich et al. (2010).

CONCLUSIONS

We have developed an analytical model for seismic attenuation and dispersion in a fluid-saturated porous medium caused by squirt flow. We used the classical pore space geometry used in many previous studies, a penny-shaped crack surrounded by a toroidal stiff pore. Our model can be applied to very thin cracks as well as to cracks with finite thicknesses. We compared our analytical model with three-dimensional numerical solutions. The analytical and numerical results are in a very good agreement for all considered relative sizes of pores and cracks. Our analytical model features several key differences compared with previously published analytical models making it much more accurate. First, we provide an approach to calculate the elastic moduli of interconnected pore and crack. We showed that ignoring the inter-connectivity of cracks and pores in the calculation of the model compliance leads to inaccurate predictions of low- and high- frequency limits of the moduli dispersion. Second, we derived a good approximation for the relaxation of the crack stiffness due to fluid pressure diffusion, which makes our model accurate for the whole frequency band. Furthermore, we showed that the crack stiffness is significantly affected by the surrounding heterogenities. Thus, precise expressions for the crack stiffness are possible only for specific pore geometries.

Figures

Tables

ACKNOWLEDGMENTS

This research is funded by the Swiss National Science Foundation, project number 172691. Yury Alkhimenkov gratefully acknowledge additional support from the Ministry of Science and Higher Education of the Russian Federation (project No. 075-15-2019-1890). We thank Boris Gurevich, Josef Paffenholz, Yury Podladchikov and an anonymous reviewer for many valuable suggestions and recommendations. The authors thank Philippe Logean for technical support and the Swiss Geocomputing Centre for providing computational resources. No data were used in producing this manuscript. The routines archive (v1.0) (Alkhimenkov and Quintal, 2021) is available from a permanent DOI repository (Zenodo) at `http://doi.org/10.5281/zenodo.5752570` (last access: 3 December 2021).

APPENDIX A

NUMERICAL METHODOLOGY

The numerical methodology we use for validation of the analytical models is described by Quintal et al. (2019) and Alkhimenkov et al. (2020a,b), here we briefly outline the main equations. We consider that a model is composed by a solid material (grains) and a pore space saturated with a fluid. The solid phase is described as a linear isotropic elastic

material for which the conservation of momentum is (e.g., Landau and Lifshitz (1959b) and Nemat-Nasser and Hori (2013))

$$\nabla \cdot \boldsymbol{\sigma} = 0, \tag{A-1}$$

where "$\nabla \cdot$" stands for the divergence operator acting on the stress tensor $\boldsymbol{\sigma}$. The infinitesimal stress-strain relation for an isotropic elastic material can be written as

$$\boldsymbol{\sigma} = (K - \frac{2}{3}\mu)\mathbf{tr}\left(\frac{1}{2}\left((\nabla \otimes \mathbf{u}) + (\nabla \otimes \mathbf{u})^{\mathrm{T}}\right)\right)\mathbf{I}_2 + 2\mu\left(\frac{1}{2}\left((\nabla \otimes \mathbf{u}) + (\nabla \otimes \mathbf{u})^{\mathrm{T}}\right)\right), \tag{A-2}$$

where $\mathbf{I}_2$ is the second order identity tensor, $\mathbf{tr}$ is the trace operator, "$\otimes$" denotes the tensor product, the superscript "T" corresponds to the transpose operator, $\mathbf{u}$ is the displacement vector, K and μ are the bulk and shear moduli, respectively. The fluid phase is described by the quasi-static linearised compressible Navier-Stokes momentum equation (Landau and Lifshitz, 1959a):

$$-\nabla p + \eta\nabla^2\mathbf{v} + \frac{1}{3}\eta\nabla\left(\nabla \cdot \mathbf{v}\right) = 0, \tag{A-3}$$

where $\mathbf{v}$ is the particle velocity, p is the fluid pressure and η is the shear viscosity. Equation (A-3) is valid for the laminar flow of a Newtonian fluid. In the numerical solver, equations (A-2)-(A-3) are written in the space-frequency domain as

$$\sigma_{ij} = \lambda e\delta_{ij} + 2\mu\epsilon_{ij} + \boldsymbol{i}\omega\left(2\eta\epsilon_{ij} - \frac{2}{3}\eta e\delta_{ij}\right), \tag{A-4}$$

where ϵ_{ij} are the components of the strain tensor $\epsilon_{ij} = 0.5\left(u_{i,j} + u_{j,i}\right)$, e is the trace of the strain tensor, λ and μ are the Lame parameters, u_i is the displacement in the i-th direction, δ_{ij} is the Kronekecker delta, $\boldsymbol{i}$ is the imaginary unit and ω is the angular frequency. Equations (A-1) and (A-4) are implemented into a finite-element solver. In the domain representing a solid material, the equation (A-4) reduces to equation (A-2) by setting the shear viscosity η to zero. In the domain representing compressible viscous fluid, equation (A-3) is recovered by setting the shear modulus μ to zero. The solid and fluid displacements are described by the same variable and, thus, naturally coupled at the boundaries between subdomains (Quintal et al., 2016, 2019). The numerical model is discretized using an unstructured mesh with tetrahedral elements (Figure A-1). A direct PARDISO solver (Schenk and Gärtner, 2004) is used for solving the linear system of equations.

Direct relaxation tests are performed to compute all components of the stiffness matrix C_{ij} (Voigt notation) by applying a displacement boundary condition of the form $u = 10^{-8} \times \exp(\boldsymbol{i}\omega t)$ to a certain external wall of the model and in a certain direction, while at other walls of the model, the displacements are set to zero or let free to change. In the direct tests that we perform, only one component of the stiffness matrix c_{ij} can be directly calculated after one numrical simulation. A detailed description of the boundary conditions is given in Alkhimenkov et al. (2020a,b). The resulting stress and strains are averaged over the spatial domain for each frequency. Then, the complex valued $C_{ii}(\omega)$ components (diagonal) are calculated for each frequency (in Voigt notation, no index summation):

$$C_{ii}(\omega) = \frac{\langle\sigma_i(\omega)\rangle}{\langle\epsilon_i(\omega)\rangle}, \tag{A-5}$$

where $\langle\cdot\rangle$ represents the volume averaging over the sample volume. For calculating the P-wave modulus ($ii = 11, 22, 33$), a harmonic displacement on the i direction is applied perpendicularlly to a wall of the model. At the other walls of the model, the normal component of the displacement is set to zero. For calculating shear components of the stiffness matrix ($ii = 44, 55, 66$), the boundary conditions applied are those of a simple shear test. For the $C_{12}(\omega)$, $C_{13}(\omega)$ and $C_{23}(\omega)$ components (off-diagonal), mixed direct tests are performed. The corresponding inverse quality factor is (O'Connell and Budiansky, 1978)

$$\frac{1}{Q_{ij}(\omega)} = \frac{\mathrm{Im}\left(C_{ij}(\omega)\right)}{\mathrm{Re}\left(C_{ij}(\omega)\right)}, \tag{A-6}$$

which is used as a measure of attenuation (O'Connell and Budiansky, 1978). In the simulations, the energy dissipation is caused by fluid pressure diffusion. The viscous shear relaxation in the fluid (O'Connell and Budiansky, 1977) is negligible in our study.

APPENDIX B

ANALYTICAL MODEL OF COLLET AND GUREVICH (2016)

We compare the results of our numerical simulation against an anisotropic version of the squirt flow analytical solution of Gurevich et al. (2010) proposed by Collet and Gurevich (2016). Here we use the formulation presented by Alkhimenkov et al. (2020a). Collet and Gurevich (2016) consider a double-porosity medium with aligned identical cracks embedded in a hypothetical background rock matrix made up of grains and stiff pores only. The crack is fully described in terms of normal and tangential compliances Z_n and Z_t, respectively (Kachanov, 1993; Schoenberg and Sayers, 1995; Sayers and Kachanov, 1995). They consider the so-called modified frame in which only the cracks are filled with fluid, whereas the stiffer pores are empty (Mavko and Jizba, 1991). In the low frequency limit, the relaxed moduli of the modified frame are equal to the rock dry moduli (which means that $Z_n^{\mathrm{MF}} = Z_n$); while in the high frequency limit, the fluid in the cracks stiffens the frame and the unrelaxed moduli of the modified frame are equal to the dry moduli of the rock without a compliant porosity (which means that $Z_n^{\mathrm{MF}} = 0$) (Mavko and Jizba, 1991).

In the analytical solution of Collet and Gurevich (2016), the frequency dependent compliance tensor of the modified frame is written as (for a vertical transversely isotropic (VTI) medium)

$$S_{mn}^{\mathrm{MF}}(\omega) = S_{mn}^{b} + \Delta S_{mn}^{\mathrm{MF}}(\omega), \tag{B-1}$$

where S_{mn}^{b} is the compliance tensor of the rock matrix, and $\Delta S_{mn}^{\mathrm{MF}}(\omega)$ is the additional

compliance due to the crack (Schoenberg and Helbig, 1997):

$$\Delta S_{mn}^{\mathrm{MF}}(\omega) = \begin{bmatrix} 0 & 0 & 0 & 0 & 0 & 0 \\ 0 & 0 & 0 & 0 & 0 & 0 \\ 0 & 0 & Z_n^{\mathrm{MF}}(\omega) & 0 & 0 & 0 \\ 0 & 0 & 0 & Z_t & 0 & 0 \\ 0 & 0 & 0 & 0 & Z_t & 0 \\ 0 & 0 & 0 & 0 & 0 & 0 \end{bmatrix}. \tag{B-2}$$

The frequency-dependent normal fracture compliance is

$$Z_n^{\mathrm{MF}}(\omega) = \frac{Z_n}{1 + \frac{Z_n}{\phi_c(1/K_f^*(\omega) - 1/K_g)}}, \tag{B-3}$$

where ϕ_c is the compliant porosity (crack porosity), Z_n is the normal compliance of the crack. Gurevich et al. (2010) proposed that the stiffness of the crack can be described using a frequency-dependent fluid bulk modulus $K_f^*(\omega)$:

$$K_f^*(\omega) = \left[1 - \frac{2J_1(ka)}{kaJ_0(kr)}\right] K_f, \tag{B-4}$$

where J_ξ is Bessel function of the first kind ($\xi = 0$ or $\xi = 1$ correspond to the zero or first order Bessel function), K_f is the fluid bulk modulus, a is the radius of the crack, k is the wavenumber of the pressure wave:

$$ka = \frac{1}{\alpha}\left(-\frac{3i\omega\eta}{K_f}\right)^{1/2}, \tag{B-5}$$

α is the aspect ratio of the crack (crack thickness divided by diameter) and η is the viscosity of the fluid. Equations (B-4)-(B-5) were obtained by imposing a zero fluid pressure boundary condition ($P_f = 0$) at the edge of the cylindrical crack (Gurevich et al., 2010). The frequency-dependent stiffness tensor of the fluid saturated medium is given by the anisotropic Gassmann's equation (Gassmann, 1951):

$$C_{mn}^{\mathrm{sat}}(\omega) = C_{mn}^{\mathrm{MF}}(\omega) + \alpha_m \alpha_n M, \tag{B-6}$$

$$\alpha_m = 1 - \left(\sum_{n=1}^{3} C_{mn}^{\mathrm{MF}}\right)\beta_g/3, \tag{B-7}$$

for $m = 1, 2, 3$ and $\alpha_4 = \alpha_5 = \alpha_6 = 0$, and where

$$M = \left(\phi\beta_f + (1-\phi)\beta_g - K^*\beta_g^2\right)^{-1}, \tag{B-8}$$

$$K^* = \frac{1}{9}\sum_{m=1}^{3}\sum_{n=1}^{3} C_{mn}^{\mathrm{MF}}(\omega), \tag{B-9}$$

ϕ is the total porosity of the medium without the compliant porosity, K^* is the generalized bulk modulus of the modified frame, β_f is the compressibility of the fluid, α_m is the Biot-Willis coefficient, β_g is the compressibility of the grain material.

For the comparison between the analytical solution and the numerical results, all stiffness properties of the dry medium are calculated numerically (or are the same as in the numerical simulation) and used as input to the analytical solution. In order to obtain the normal Z_n and tangential Z_t compliances of the crack we numerically calculate several (homogenized) elastic stiffness tensors of a dry medium (Figure B-1): a torus embedded into the solid grain material (C_1^{VTI} stiffness tensor); a crack embedded into a medium described by the C_1^{VTI} stiffness tensor (C_2^{VTI} stiffness tensor); a torus connected with a crack embedded into the solid grain material (C_3^{VTI} stiffness tensor). Then, all C^{VTI} stiffness tensors are inverted to the corresponding compliance tensors S^{VTI}. For obtaining Z_n and Z_t there are two options:

Workflow A) Z_n and Z_t are calculated using the difference between the S_1^{VTI} compliance tensor and the S_2^{VTI} compliance tensor (Figure B-1). In this case, we first homogenize the torus (and obtain C_1^{VTI}) and then, embed the crack into this homogenized material C_1^{VTI}. Thus, Z_n and Z_t do not take into account the fact that the crack is connected with the stiffer pore. This approach is used by Collet and Gurevich (2016).

Workflow B) Z_n and Z_t are calculated using the difference between the S_1^{VTI} compliance tensor and the S_3^{VTI} compliance tensor (Figure B-1). In this case, we also first homogenize the torus but then, embed the crack connected to the torus into the solid grain material. Thus, the C_3^{VTI} stiffness tensor corresponds to the dry stiffness tensor of the model, so the difference $S_1^{VTI} - S_3^{VTI}$ gives the correct compliances Z_n and Z_t for the dry model (using the the homogenized material C_1^{VTI}).

REFERENCES

Adelinet, M., J. Fortin, Y. Guéguen, A. Schubnel, and L. Geoffroy, 2010, Frequency and fluid effects on elastic properties of basalt: Experimental investigations: Geophysical Research Letters, **37**.

Alkhimenkov, Y., E. Caspari, B. Gurevich, N. D. Barbosa, S. Glubokovskikh, J. Hunziker, and B. Quintal, 2020a, Frequency-dependent attenuation and dispersion caused by squirt flow: Three-dimensional numerical study: Geophysics, **85**, MR129–MR145.

Alkhimenkov, Y., E. Caspari, S. Lissa, and B. Quintal, 2020b, Azimuth-, angle-and frequency-dependent seismic velocities of cracked rocks due to squirt flow: Solid Earth, **11**, 855–871.

Alkhimenkov, Y., and B. Quintal, 2021, Attenuation_part_1.

Borgomano, J. V., L. X. Pimienta, J. Fortin, and Y. Guéguen, 2019, Seismic dispersion and attenuation in fluid-saturated carbonate rocks: Effect of microstructure and pressure: Journal of Geophysical Research: Solid Earth, **124**, 12498–12522.

Carcione, J. M., and B. Gurevich, 2011, Differential form and numerical implementation of biot's poroelasticity equations with squirt dissipation: Geophysics, **76**, N55–N64.

Chalhoub, M. S., and J. M. Kelly, 1990, Effect of bulk compressibility on the stiffness of cylindrical base isolation bearings: International Journal of Solids and Structures, **26**, 743–760.

Chapman, M., 2003, Frequency-dependent anisotropy due to meso-scale fractures in the presence of equant porosity: Geophysical Prospecting, **51**, 369–379.

Chapman, M., S. V. Zatsepin, and S. Crampin, 2002, Derivation of a microstructural poroelastic model: Geophysical Journal International, **151**, 427–451.

Chapman, S., J. V. Borgomano, H. Yin, J. Fortin, and B. Quintal, 2019, Forced oscillation measurements of seismic wave attenuation and stiffness moduli dispersion in glycerine-saturated berea sandstone: Geophysical Prospecting, **67**, 956–968.

Collet, O., and B. Gurevich, 2016, Frequency dependence of anisotropy in fluid saturated rocks–part i: aligned cracks case: Geophysical Prospecting, **64**, 1067–1084.

Das, V., T. Mukerji, and G. Mavko, 2019, Numerical simulation of coupled fluid-solid interaction at the pore scale: A digital rock-physics technology: Geophysics, **84**, no. 4, WA71–WA81.

Dvorkin, J., G. Mavko, and A. Nur, 1995, Squirt flow in fully saturated rocks: Geophysics, **60**, 97–107.

Dvorkin, J., and A. Nur, 1993, Dynamic poroelasticity: A unified model with the squirt and the biot mechanisms: Geophysics, **58**, 524–533.

Gassmann, F., 1951, Über die elastizität poröser medien: Vierteljahrsschrift der Naturforschenden Gesellschaft in Zürich, **96**, 1–23.

Glubokovskikh, S., B. Gurevich, and N. Saxena, 2016, A dual-porosity scheme for fluid/solid substitution: Geophysical Prospecting, **64**, 1112–1121.

Gurevich, B., 2003, Elastic properties of saturated porous rocks with aligned fractures: Journal of Applied Geophysics, **54**, 203–218.

Gurevich, B., M. Brajanovski, R. J. Galvin, T. M. Müller, and J. Toms-Stewart, 2009, P-wave dispersion and attenuation in fractured and porous reservoirs–poroelasticity approach: Geophysical Prospecting, **57**, 225–237.

Gurevich, B., D. Makarynska, O. B. de Paula, and M. Pervukhina, 2010, A simple model for squirt-flow dispersion and attenuation in fluid-saturated granular rocks: Geophysics, **75**, N109–N120.

Hashin, Z., 1970, Complex moduli of viscoelastic composites—i. general theory and application to particulate composites: International Journal of Solids and Structures, **6**, 539–552.

Jakobsen, M., and M. Chapman, 2009, Unified theory of global flow and squirt flow in cracked porous media: Geophysics, **74**, WA65–WA76.

Johnson, D. L., 2001, Theory of frequency dependent acoustics in patchy-saturated porous media: The Journal of the Acoustical Society of America, **110**, 682–694.

Jones, T. D., 1986, Pore fluids and frequency-dependent wave propagation in rocks: Geophysics, **51**, 1939–1953.

Kachanov, M., 1993, Elastic solids with many cracks and related problems: Elsevier, **30**, 259–445.

Kachanov, M., and I. Sevostianov, 2018, Micromechanics of materials, with applications: Springer, **249**.

Landau, L., and E. Lifshitz, 1959a, Course of theoretical physics. vol. 6: Fluid mechanics: London.

Landau, L. D., and E. M. Lifshitz, 1959b, Course of theoretical physics vol 7: Theory and elasticity: Pergamon press.

Lissa, S., N. D. Barbosa, E. Caspari, Y. Alkhimenkov, and B. Quintal, 2020, Squirt flow in cracks with rough walls: Journal of Geophysical Research: Solid Earth, **125**, e2019JB019235.

Lissa, S., M. Ruf, H. Steeb, and B. Quintal, 2021, Digital rock physics applied to squirt flow: Geophysics, **86**, 1–40.

Madonna, C., B. Quintal, M. Frehner, B. S. Almqvist, N. Tisato, M. Pistone, F. Marone, and E. H. Saenger, 2013, Synchrotron-based x-ray tomographic microscopy for rock physics investigations: Geophysics, **78**, D53–D64.

Mavko, G., and D. Jizba, 1991, Estimating grain-scale fluid effects on velocity dispersion in rocks: Geophysics, **56**, 1940–1949.

Mavko, G., T. Mukerji, and J. Dvorkin, 2009, The rock physics handbook: Tools for seismic analysis of porous media: Cambridge university press.

———, 2020, The rock physics handbook: Cambridge university press.

Mavko, G., and A. Nur, 1975, Melt squirt in the asthenosphere: Journal of Geophysical Research, **80**, 1444–1448.

Mayr, S. I., and H. Burkhardt, 2006, Ultrasonic properties of sedimentary rocks: effect of pressure, saturation, frequency and microcracks: Geophysical Journal International, **164**, 246–258.

Mikhaltsevitch, V., M. Lebedev, and B. Gurevich, 2015, A laboratory study of attenuation and dispersion effects in glycerol-saturated berea sandstone at seismic frequencies, *in* SEG Technical Program Expanded Abstracts 2015: Society of Exploration Geophysicists, 3085–3089.

Mukerji, T., and G. Mavko, 1994, Pore fluid effects on seismic velocity in anisotropic rocks: Geophysics, **59**, 233–244.

Müller, T. M., B. Gurevich, and M. Lebedev, 2010, Seismic wave attenuation and dispersion resulting from wave-induced flow in porous rocks—a review: Geophysics, **75**, 75A147–75A164.

Murphy, W. F., K. W. Winkler, and R. L. Kleinberg, 1986, Acoustic relaxation in sedimentary rocks: Dependence on grain contacts and fluid saturation: Geophysics, **51**, 757–766.

Nemat-Nasser, S., and M. Hori, 2013, Micromechanics: overall properties of heterogeneous materials: Elsevier.

O'Connell, R., and B. Budiansky, 1978, Measures of dissipation in viscoelastic media: Geophysical Research Letters, **5**, 5–8.

O'Connell, R. J., and B. Budiansky, 1977, Viscoelastic properties of fluid-saturated cracked solids: Journal of Geophysical Research, **82**, 5719–5735.

Palmer, I., and M. Traviolia, 1980, Attenuation by squirt flow in undersaturated gas sands: Geophysics, **45**, 1780–1792.

Pimienta, L., J. Fortin, and Y. Guéguen, 2015a, Bulk modulus dispersion and attenuation in sandstones: Geophysics, **80**, D111–D127.

———, 2015b, Experimental study of young's modulus dispersion and attenuation in fully saturated sandstones: Geophysics, **80**, L57–L72.

Pride, S. R., J. G. Berryman, and J. M. Harris, 2004, Seismic attenuation due to wave-induced flow: Journal of Geophysical Research: Solid Earth, **109**.

Pride, S. R., F. D. Morgan, and A. F. Gangi, 1993, Drag forces of porous-medium acoustics: Physical review B, **47**, 4964.

Quintal, B., E. Caspari, K. Holliger, and H. Steeb, 2019, Numerically quantifying energy loss caused by squirt flow: Geophysical Prospecting. (doi:10.1111/1365-2478.12832).

Quintal, B., J. G. Rubino, E. Caspari, and K. Holliger, 2016, A simple hydromechanical approach for simulating squirt-type flow: Geophysics, **81**, D335–D344.

Sayers, C., and M. Kachanov, 1995, Microcrack-induced elastic wave anisotropy of brittle rocks: Journal of Geophysical Research: Solid Earth, **100**, 4149–4156.

Schenk, O., and K. Gärtner, 2004, Solving unsymmetric sparse systems of linear equations with pardiso: Future Generation Computer Systems, **20**, 475–487.

Schoenberg, M., and J. Douma, 1988, Elastic wave propagation in media with parallel fractures and aligned cracks1: Geophysical prospecting, **36**, 571–590.

Schoenberg, M., and K. Helbig, 1997, Orthorhombic media: Modeling elastic wave behavior in a vertically fractured earth: Geophysics, **62**, 1954–1974.

Schoenberg, M., and C. M. Sayers, 1995, Seismic anisotropy of fractured rock: Geophysics, **60**, 204–211.

Solazzi, S. G., S. Lissa, J. G. Rubino, and K. Holliger, 2021, Squirt flow in partially saturated cracks: a simple analytical model: Geophysical Journal International, **227**, 680–692.

Subramaniyan, S., B. Quintal, C. Madonna, and E. H. Saenger, 2015, Laboratory-based seismic attenuation in fontainebleau sandstone: Evidence of squirt flow: Journal of Geophysical Research: Solid Earth, **120**, 7526–7535.

Tsai, H.-C., and C.-C. Lee, 1998, Compressive stiffness of elastic layers bonded between rigid plates: International Journal of Solids and Structures, **35**, 3053–3069.

Xu, S., 1998, Modelling the effect of fluid communication on velocities in anisotropic porous rocks: International Journal of Solids and Structures, **35**, 4685–4707.

Zhang, Y., L. Song, M. Deffenbaugh, and M. N. Toksöz, 2010, A finite difference method for a coupled model of wave propagation in poroelastic materials: The Journal of the Acoustical Society of America, **127**, 2847–2855.

Zhang, Y., and M. N. Toksöz, 2012, Computation of dynamic seismic responses to viscous fluid of digitized three-dimensional berea sandstones with a coupled finite-difference method: The Journal of the Acoustical Society of America, **132**, 630–640.

LIST OF TABLES

1 Geometrical properties for the Big pore model and the Small pore model. Major radius — the distance from the center of the tube to the center of the torus. Minor radius — the radius of the tube (our isometric pore).

2 Material properties used in all models.

LIST OF FIGURES

1 Workflow to (i) benchmark published analytical models and (ii) ensure the quality of future models.

2 Raw synchrotron radiation X-ray tomographic microscopy image of dry Berea sandstone. One slice of the total data cube with 1024^3 voxels [from Madonna et al. (2013)].

3 The development of the present analytical model.

4 (a) Sketch illustrating the Big pore model: a flat cylinder representing a crack whose edge is connected to a torus representing a stiff isometric pore. (b) A vertical slice across half of the model. r is the minor radius of the torus ($d_{Mn} = 2r$ is the minor diameter of the torus), $d_{Mj} = r + b$ is the major radius of the torus.

5 Cartoon illustrating the different model configurations used to obtain the corresponding compliance matrices.

6 Sketch illustrating the configurations of our model that corresponds to the high- and low-frequency limits obtained from the numerical calculations for the $[C^*_{33}]_{\text{sat}}$ component (properties in Tables 1 and 2).

7 Sketch illustrating the workflow for calculating analytically different components of the compliance matrix for the model with interconnected isometric pore and crack.

8 Sketch illustrating the simplifications made in analytical models via applied boundary conditions (a vertical slice of the two models shown in Figure 4). Panels a) and c) — boundary conditions applied to the walls of the model. Panels b) and d) — boundary conditions applied to the walls of the crack. Panel e) shows the numerical result; note, that the high-frequency slope of the attenuation curve is substantially different if the crack is connected to an actual pore.

9 The real part of the frequency-dependent fluid bulk modulus K^*_f and the dimensionless attenuation calculated using different expressions for the Big pore model with $\alpha = 0.005$.

10 The real part of the frequency-dependent fluid bulk modulus K^*_f and the dimensionless attenuation calculated using different expressions for the Big pore model with $\alpha = 0.005$.

11 The real part of the frequency-dependent fluid bulk modulus K^*_f and the dimensionless attenuation calculated using different expressions for the Small pore model with $\alpha = 0.0025$.

12 Numerical and analytical results for the Big pore model (Figure 4) with a crack aspect ratio $\alpha = 0.0025$: (a) Real part of the $[C^*_{33}]_{\text{sat}}$ component and (b) dimensionless attenuation for the $[C^*_{33}]_{\text{sat}}$ component. On the right, snapshots of the fluid pressure P_f at three different frequencies : LF - low frequency limit (relaxed state), Fc - intermediate frequency (close to the characteristic frequency) and HF - high frequency limit (unrelaxed state). The spatial dimension of the snapshots are not-to-scale and their colors representing the fluid pressure P_f correspond to a downward displacement (compression) of 10^{-8}m applied to the top boundary of the model. The inset represents the cross section of half of the model.

13 Numerical and analytical results for the Big pore model with the crack aspect ratio $\alpha = 0.005$ (i.e., finite thickness crack): (a) Real part of the $[C^*_{33}]_{\text{sat}}$ component and (b)

dimensionless attenuation for the $[C^*_{33}]_{\text{sat}}$ component. Here the crack aperture is two times larger than in the model with aspect ratio of $\alpha = 0.0025$ (Figure 12). The inset represents the cross section of half of the model.

14 Numerical and analytical results for the modified frame of the Big pore model with the crack aspect ratio $\alpha = 0.005$ (i.e., finite thickness crack): (a) Real part of the $[C^*_{33}]^{\text{MF}}$ component and (b) dimensionless attenuation for the $[C^*_{33}]^{\text{MF}}$ component. The inset represents the cross section of half of the model.

15 Numerical and analytical results for the modified frame of the Small pore model with the crack aspect ratio $\alpha = 0.0025$: (a) Real part of the $[C^*_{33}]^{\text{MF}}$ component and (b) dimensionless attenuation for the $[C^*_{33}]^{\text{MF}}$ component. The inset represents the cross section of half of the model.

16 A slice of the three-dimensional models illustrating the effect of elastic interactions on the $[C^*_{33}]_{\text{dry}}$ component. (a) The isometric pore is connected to the crack representing a unified interconnected pore space, (b) the isometric pore and crack are disconnected but close and (c) disconnected and far from each other.

17 Sketch illustrating the pore space (dry) of the Big pore model with two different crack apertures — h (left) and $50h$ (right).

18 Numerical and analytical results for the big pore model with the crack aspect ratio $\alpha = 0.025$: (a) Real part of the $[C^*_{33}]_{\text{sat}}$ component and (b) dimensionless attenuation for the $[C^*_{33}]_{\text{sat}}$ component.

A-1 The element's size distribution for the Big pore model. The element's size in the crack is $\approx 6 \times 10^{-4}$ m, and in the surrounding grain material it is $7.2 \times 10^{-3} - 4 \times 10^{-2}$ m. The element's size distribution for the other models is similar. The total number of elements is $1.5 \times 10^6 - 5 \times 10^6$ depending on the model configuration, e.g., Big/Small pore or full/half/quarter of a model was used.

B-1 Sketch illustrating the calculation of normal and tangential compliances of the crack for workflows A and B. S_r^{VTI} denotes the compliance tensor, which is the inverse of the corresponding stiffness tensor, i.e., $S_r^{VTI} = (C_r^{VTI})^{-1}$, for $r = 1, 2, 3$. The resulting Z_n and Z_t are used to calculate the analytical solution for corresponding models.

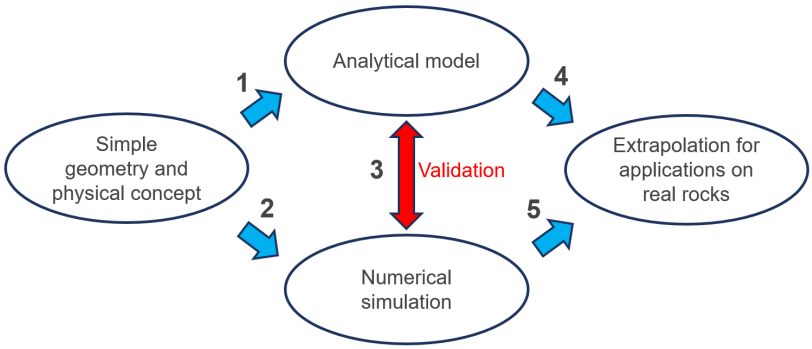

Figure 1: Workflow to (i) benchmark published analytical models and (ii) ensure the quality of future models.

Alkhimenkov Y. and Quintal B. –

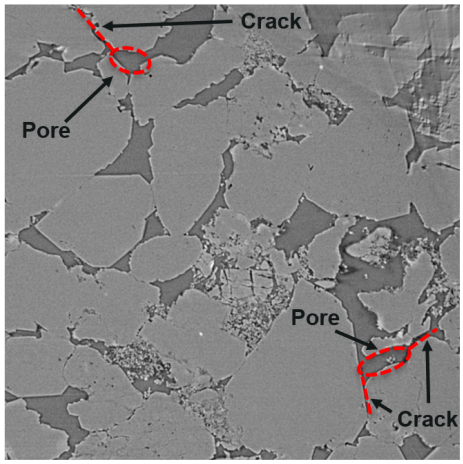

Figure 2: Raw synchrotron radiation X-ray tomographic microscopy image of dry Berea sandstone. One slice of the total data cube with 1024^3 voxels [from Madonna et al. (2013)].

Alkhimenkov Y. and Quintal B. –

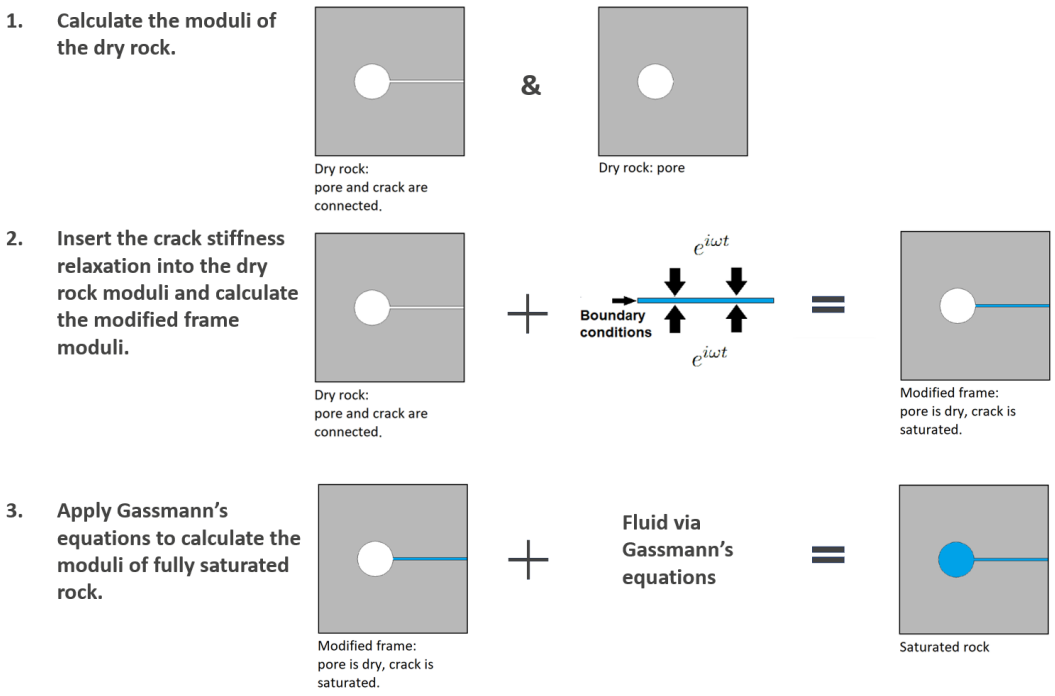

Figure 3: The development of the present analytical model.

Alkhimenkov Y. and Quintal B. –

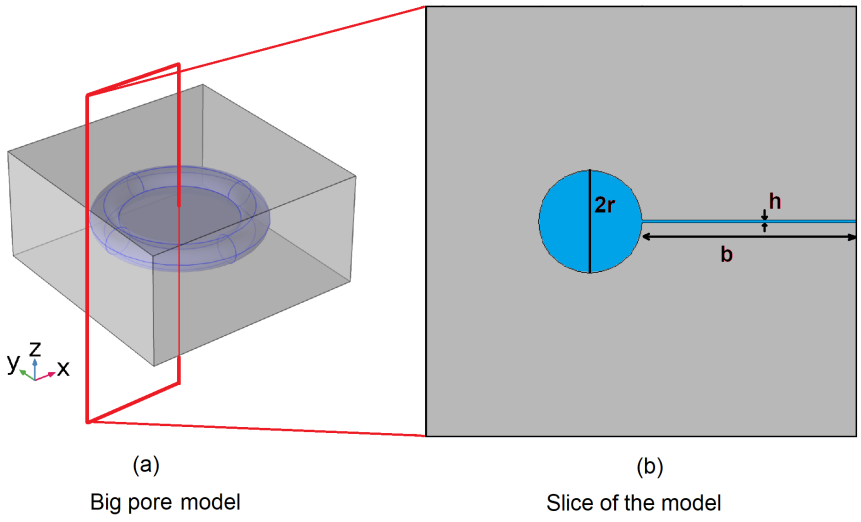

Figure 4: (a) Sketch illustrating the Big pore model: a flat cylinder representing a crack whose edge is connected to a torus representing a stiff isometric pore. (b) A vertical slice across half of the model. r is the minor radius of the torus ($d_{Mn} = 2r$ is the minor diameter of the torus), $d_{Mj} = r + b$ is the major radius of the torus.

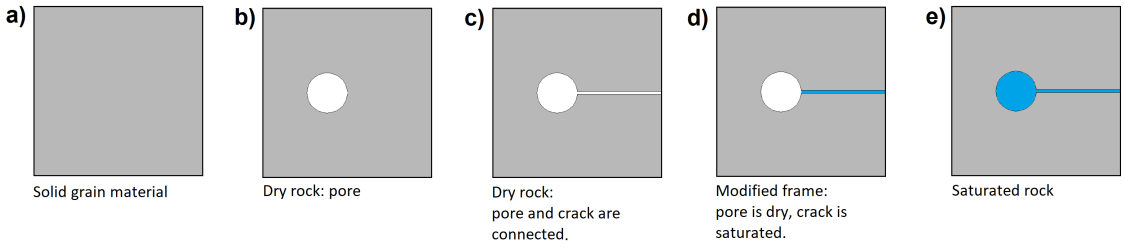

Figure 5: Cartoon illustrating the different model configurations used to obtain the corresponding compliance matrices.

Alkhimenkov Y. and Quintal B. –

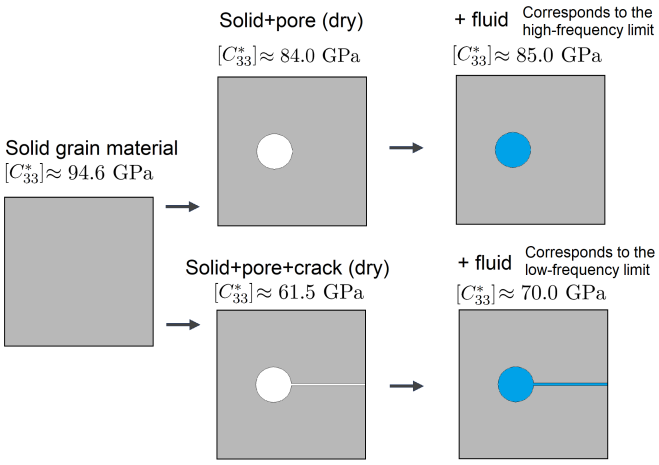

Figure 6: Sketch illustrating the configurations of our model that corresponds to the high- and low-frequency limits obtained from the numerical calculations for the $[C^*_{33}]_{\text{sat}}$ component (properties in Tables 1 and 2).

Alkhimenkov Y. and Quintal B. –

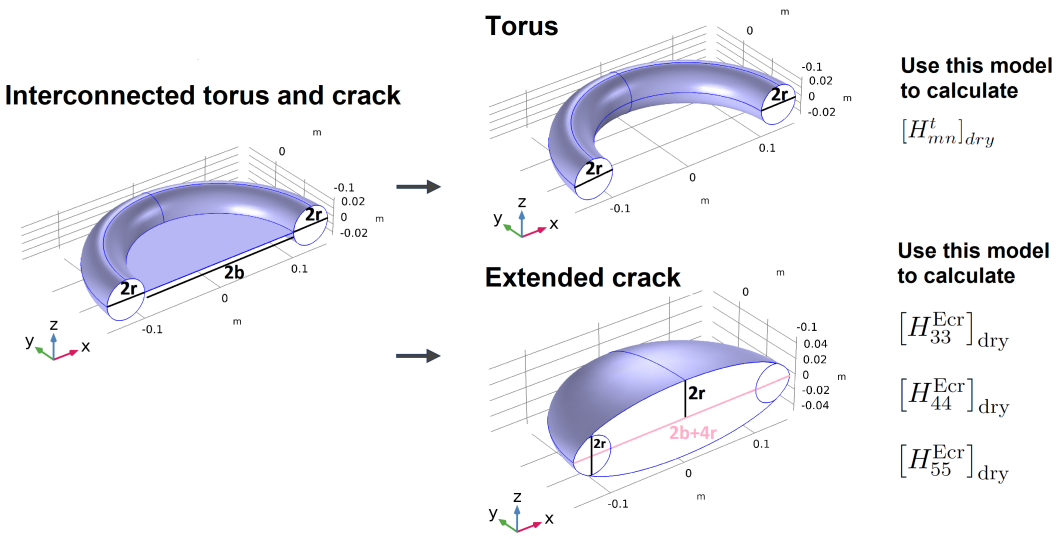

Figure 7: Sketch illustrating the workflow for calculating analytically different components of the compliance matrix for the model with interconnected isometric pore and crack.
Alkhimenkov Y. and Quintal B. –

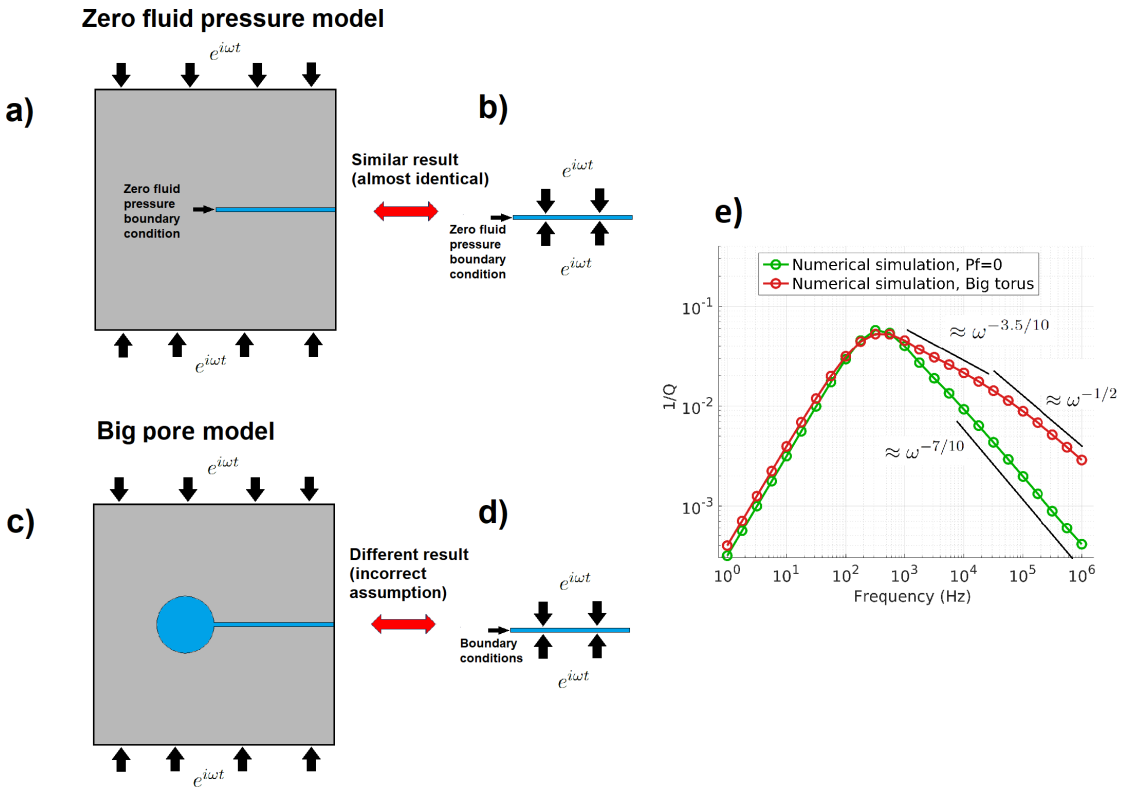

Figure 8: Sketch illustrating the simplifications made in analytical models via applied boundary conditions (a vertical slice of the two models shown in Figure 4). Panels a) and c) — boundary conditions applied to the walls of the model. Panels b) and d) — boundary conditions applied to the walls of the crack. Panel e) shows the numerical result; note, that the high-frequency slope of the attenuation curve is substantially different if the crack is connected to an actual pore.

Alkhimenkov Y. and Quintal B. –

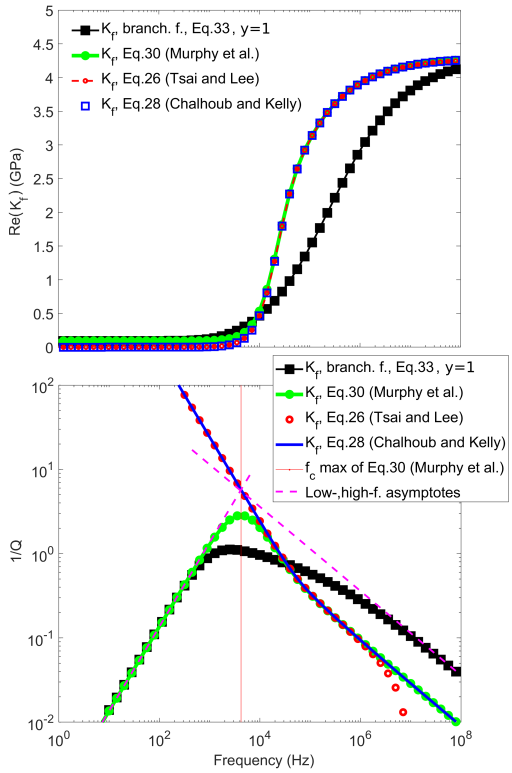

Figure 9: The real part of the frequency-dependent fluid bulk modulus K_f^* and the dimensionless attenuation calculated using different expressions for the Big pore model with $\alpha = 0.005$.

Alkhimenkov Y. and Quintal B. –

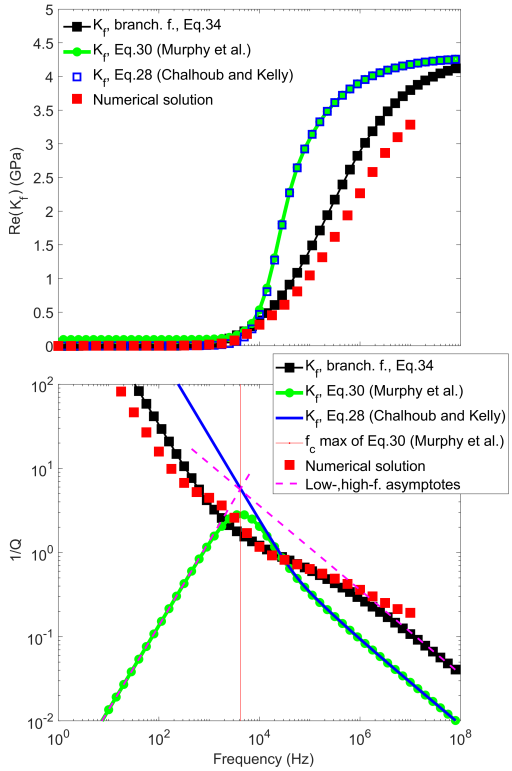

Figure 10: The real part of the frequency-dependent fluid bulk modulus K_f^* and the dimensionless attenuation calculated using different expressions for the Big pore model with $\alpha = 0.005$.

Alkhimenkov Y. and Quintal B. –

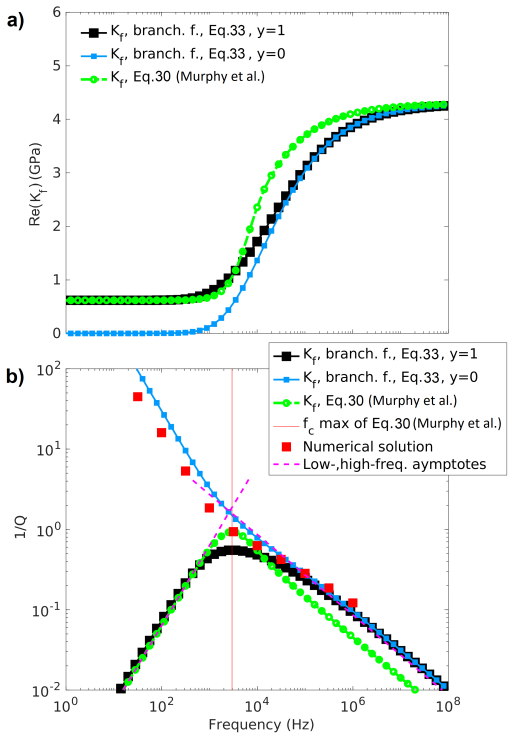

Figure 11: The real part of the frequency-dependent fluid bulk modulus K_f^* and the dimensionless attenuation calculated using different expressions for the Small pore model with $\alpha = 0.0025$.

Alkhimenkov Y. and Quintal B. –

Geometrical parameter	Big pore model	Small pore model
Flat cylinder (crack) radius, b	0.1 m	0.1 m
Flat cylinder (crack) thickness, h	0.0005 m	0.0005 m
Crack aspect ratio, $\alpha = h/(2b)$	0.0025	0.0025
Major radius of torus, $b + r$	0.124 m	0.1067 m
Minor radius of torus, r	0.024 m	0.0067 m
Total porosity	0.045	0.0034
Crack porosity	$\approx 4.9 \cdot 10^{-4}$	$\approx 4.9 \cdot 10^{-4}$

Table 1: Geometrical properties for the Big pore model and the Small pore model. Major radius — the distance from the center of the tube to the center of the torus. Minor radius — the radius of the tube (our isometric pore).

Material parameter	Solid	Fluid
Bulk modulus K	36 GPa	4.3 GPa
Shear modulus μ	44 GPa	0 GPa
Shear viscosity η	0 Pa·s	1.414 Pa·s

Table 2: Material properties used in all models.

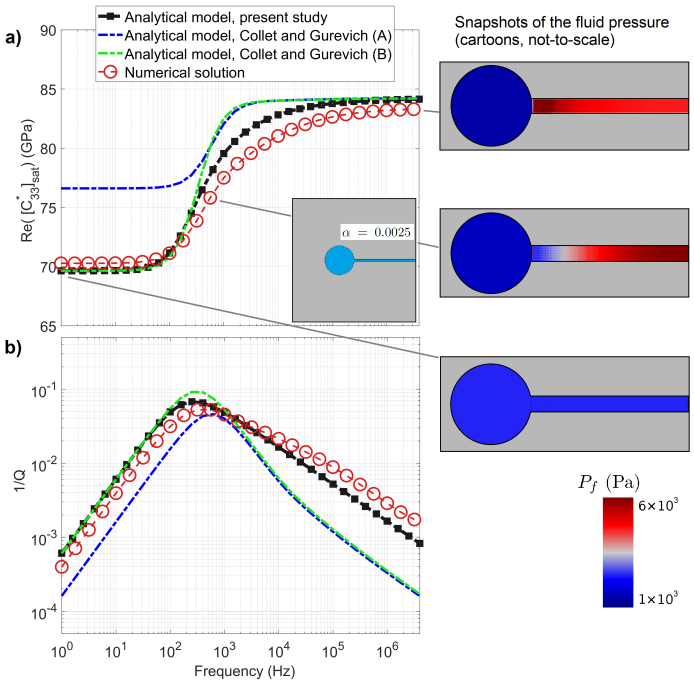

Figure 12: Numerical and analytical results for the Big pore model (Figure 4) with a crack aspect ratio $\alpha = 0.0025$: (a) Real part of the $[C^*_{33}]_{\text{sat}}$ component and (b) dimensionless attenuation for the $[C^*_{33}]_{\text{sat}}$ component. On the right, snapshots of the fluid pressure P_f at three different frequencies : LF - low frequency limit (relaxed state), Fc - intermediate frequency (close to the characteristic frequency) and HF - high frequency limit (unrelaxed state). The spatial dimension of the snapshots are not-to-scale and their colors representing the fluid pressure P_f correspond to a downward displacement (compression) of 10^{-8}m applied to the top boundary of the model. The inset represents the cross section of half of the model.

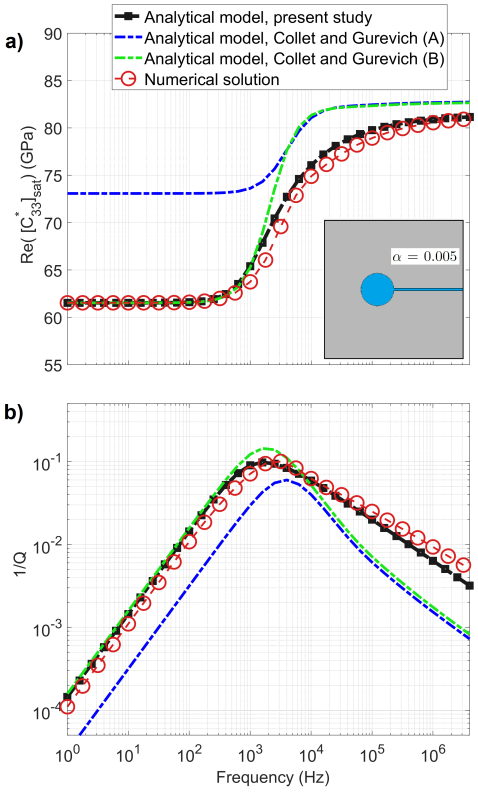

Figure 13: Numerical and analytical results for the Big pore model with the crack aspect ratio $\alpha = 0.005$ (i.e., finite thickness crack): (a) Real part of the $[C^*_{33}]_{\text{sat}}$ component and (b) dimensionless attenuation for the $[C^*_{33}]_{\text{sat}}$ component. Here the crack aperture is two times larger than in the model with aspect ratio of $\alpha = 0.0025$ (Figure 12). The inset represents the cross section of half of the model.

Alkhimenkov Y. and Quintal B. –

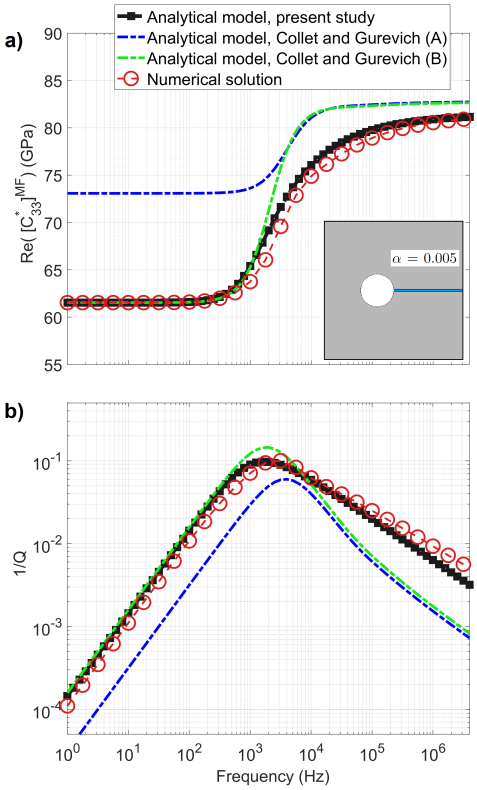

Figure 14: Numerical and analytical results for the modified frame of the Big pore model with the crack aspect ratio $\alpha = 0.005$ (i.e., finite thickness crack): (a) Real part of the $[C^*_{33}]^{\mathrm{MF}}$ component and (b) dimensionless attenuation for the $[C^*_{33}]^{\mathrm{MF}}$ component. The inset represents the cross section of half of the model.

Alkhimenkov Y. and Quintal B. –

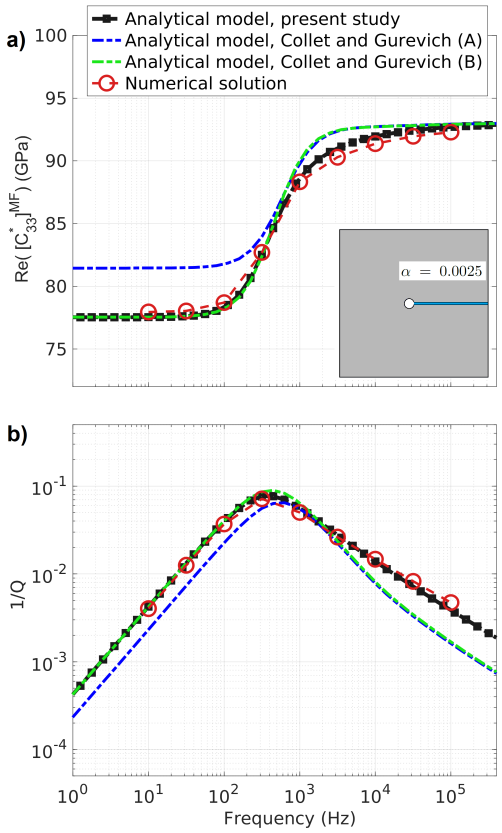

Figure 15: Numerical and analytical results for the modified frame of the Small pore model with the crack aspect ratio $\alpha = 0.0025$: (a) Real part of the $[C^*_{33}]^{\mathrm{MF}}$ component and (b) dimensionless attenuation for the $[C^*_{33}]^{\mathrm{MF}}$ component. The inset represents the cross section of half of the model.

Alkhimenkov Y. and Quintal B. –

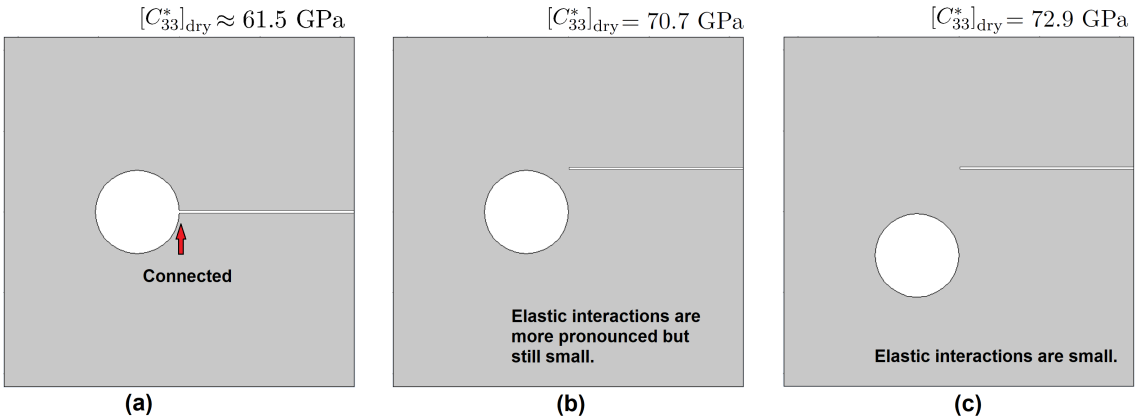

Figure 16: A slice of the three-dimensional models illustrating the effect of elastic interactions on the $[C^*_{33}]_{\rm dry}$ component. (a) The isometric pore is connected to the crack representing a unified interconnected pore space, (b) the isometric pore and crack are disconnected but close and (c) disconnected and far from each other.

Alkhimenkov Y. and Quintal B. –

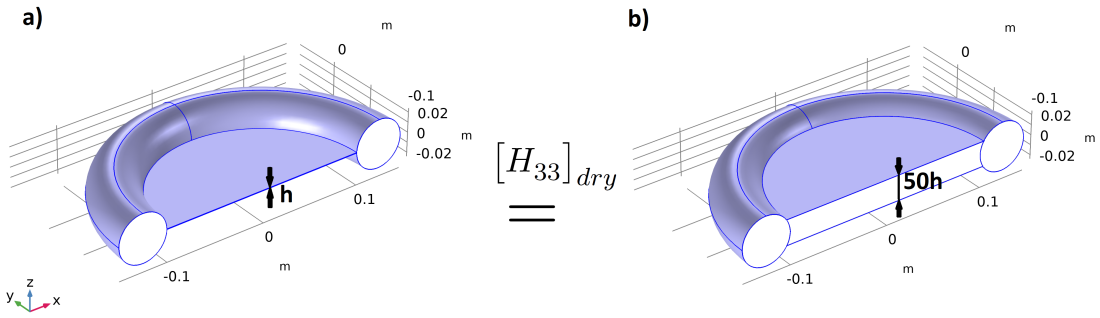

Figure 17: Sketch illustrating the pore space (dry) of the Big pore model with two different crack apertures — h (left) and $50h$ (right).

Alkhimenkov Y. and Quintal B. –

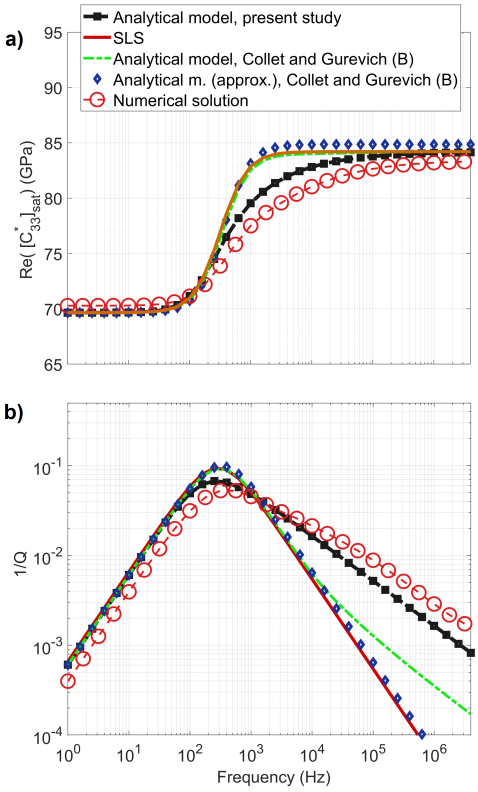

Figure 18: Numerical and analytical results for the big pore model with the crack aspect ratio $\alpha = 0.025$: (a) Real part of the $[C^*_{33}]_{\text{sat}}$ component and (b) dimensionless attenuation for the $[C^*_{33}]_{\text{sat}}$ component.

Alkhimenkov Y. and Quintal B. –

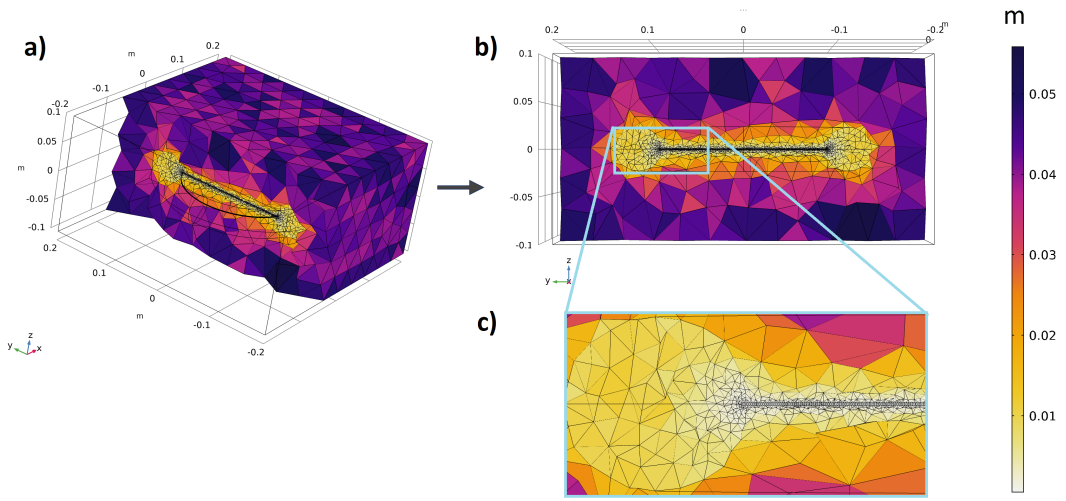

Figure A-1: The element's size distribution for the Big pore model. The element's size in the crack is $\approx 6 \times 10^{-4}$ m, and in the surrounding grain material it is $7.2 \times 10^{-3} - 4 \times 10^{-2}$ m. The element's size distribution for the other models is similar. The total number of elements is $1.5 \times 10^{6} - 5 \times 10^{6}$ depending on the model configuration, e.g., Big/Small pore or full/half/quarter of a model was used.

Alkhimenkov Y. and Quintal B. –

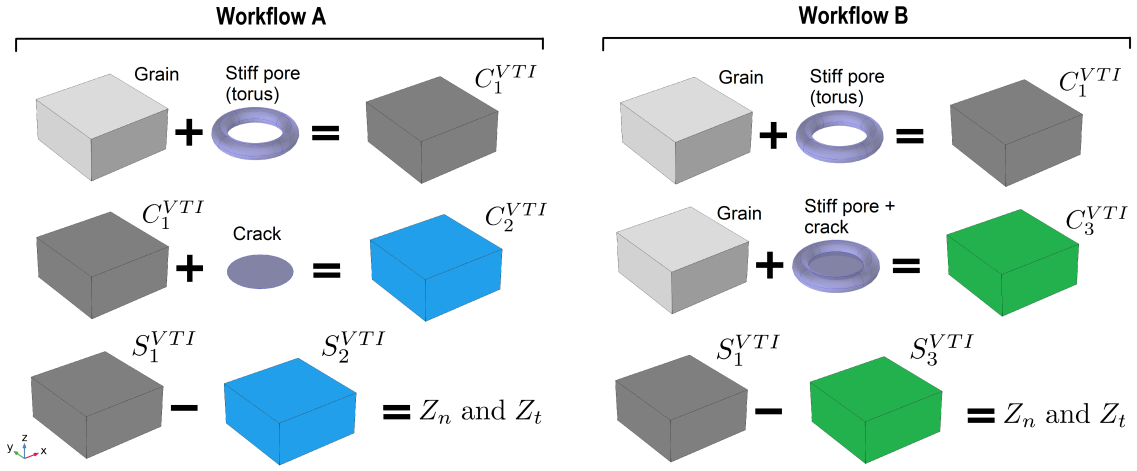

Figure B-1: Sketch illustrating the calculation of normal and tangential compliances of the crack for workflows A and B. S_r^{VTI} denotes the compliance tensor, which is the inverse of the corresponding stiffness tensor, i.e., $S_r^{VTI} = (C_r^{VTI})^{-1}$, for $r = 1, 2, 3$. The resulting Z_n and Z_t are used to calculate the analytical solution for corresponding models.

Alkhimenkov Y. and Quintal B. –